Antarctic Extreme Snowfall: A CloudSat and CALIPSO Satellite Perspective

by

Karissa Shannon

A thesis submitted in partial fulfillment
of the requirements for the degree of

Master of Science
(Atmospheric and Oceanic Sciences)

at the
University of Wisconsin-Madison
2024

Antarctic Extreme Snowfall: A CloudSat and CALIPSO Satellite Perspective

Karissa Shannon

Abstract

The Antarctic Ice Sheet is a critical component of the Earth's climate system, with its role in global sea level regulation becoming increasingly significant in a warming climate. Snowfall is a key factor in ice mass balance, influencing the ice sheet's contribution to sea level changes. Previous studies have shown that moisture intrusions can cause large snowfall events, but by focusing only on the most extreme moisture events impinging on the ice sheet, these studies only address specific regions of the ice sheet, omitting many potential mass-building snowfall events across other parts of the continent. This study examines extreme snowfall events (defined as greater than the 95th percentile) across each drainage basin in Antarctica. Using the new Combined CloudSat CALIPSO Snowfall (C3S) that leverages the snowfall detection capabilities of the CloudSat radar while mitigating errors caused by the radar blind zone with CALIPSO lidar observations, we find that top 5% of snowfall events in each basin account for nearly 40% of the total accumulation on the Antarctic ice sheet. Analyzing MERRA-2 reanalysis and automatic weather station data, we find that, unlike moderate snowfall, extreme events in many drainage basins exhibit sea level pressure dipoles that bring warm, moist air to the continent. This comprehensive analysis broadens the findings of recent work, by demonstrating that extreme snowfall events play a key role in Antarctic ice mass balance and are frequently connected to enhanced atmospheric moisture transport across the entire Antarctic ice sheet offering valuable insights for climate research and sea level rise projections.

Acknowledgements

First I would like to thank my advisor, Tristan L'Ecuyer. I have greatly appreciated his advice and encouragement throughout my master's degree.

I would also like to thank Matthew Lazzara for taking me on as a project assistant at the AMRDC. Thank you to Matthew and the rest of the AMRDC for supporting me throughout my master's and letting me explore my interests.

Thank you to Marian Mateling, who has worked on this project since the beginning and given me lots of code and advice.

Thanks to my committee Angela Rowe and Hannah Zanowski for their feedback on this thesis.

Thanks to my partner Jack, who has been amazingly supportive and cooked me yummy food during stressful times.

Thanks to all my friends who I have made in the department. My grad school experience would not be the same without them.

Last, I want to thank my family, especially my parents, who taught me to love math and science from a young age.

This work is supported by NSF grants 1951720 and 2301362 through the AMRDC + NASA CloudSat project G-3969-1.

Contents

List of Figures

List of Tables

Chapter 1

Introduction

As the earth's climate is undergoing significant change, global temperatures continue to rise with increasing greenhouse gas concentrations. This warming is causing a number of environmental changes, including rising sea level. Global mean sea level has increased by approximately 1.5 mm per year over the twentieth century, however this rate has been accelerating (Hay et al., 2015; Oppenheimer et al., 2019; Dangendorf et al., 2019). The impacts of sea level rise are far-reaching. Coastal communities around the world are at risk of flooding, which can lead to displacement, economic loss, and damage to infrastructure. Low-lying areas, such as small island nations and delta regions, are particularly vulnerable. Furthermore, sea level rise can exacerbate the effects of storm surges and high tides, increasing the frequency and severity of coastal erosion and flooding events. Some regions of the globe have already been impacted by these changes. Studies have shown that the mean tidal range in Miami, Florida has doubled since 1900 and will likely lead to chronic flooding in the near future (De Leo et al., 2022).

Sea level rise is largely driven by two processes: thermal expansion and ice mass loss (Frederikse et al., 2020). Among these mechanisms, the Greenland and

Antarctic ice sheets play a critical role as they hold most of the global fresh water (Oppenheimer et al., 2019). Between the two ice sheets, the Antarctic Ice Sheet (AIS) is the larger, covering roughly 14 million square kilometers and containing about 60% of the Earth's fresh water (Church et al., 2013). The AIS is divided into the East Antarctic Ice Sheet (EAIS) and the West Antarctic Ice Sheet (WAIS), separated by the Transantarctic Mountains that span the continent.

The stability of the AIS is crucial for maintaining the current sea level (Rignot et al., 2011). Over the past few decades, however, the AIS has shown signs of increased ice loss (Rignot et al., 2011; Shepherd et al., 2012, 2019). If the entire AIS were to melt, it would contribute 58 meters to global sea rise (Oppenheimer et al., 2019). While complete melting of the ice sheet is unlikely to occur in the near future, the melting of the AIS could contribute approximately 1.5 meters of sea level rise by the end of the 21st century (Rignot et al., 2011; Oppenheimer et al., 2019).

The annual mass loss of the AIS was approximately 120 Gt/yr from 2003 to 2019 (Smith et al., 2020). However, the AIS is experiencing increased melting primarily in its western region. The Thwaites and Pine Island glaciers, located in the Amundsen Sea Embayment of the WAIS, are particularly vulnerable, showing significant ice loss and contributing to global sea level rise (Joughin et al., 2014; Rignot et al., 2014; Gardner et al., 2018). On the other hand, the EAIS remains relatively stable, although recent extreme weather events have led to temporary gains in ice mass (Wang et al., 2023; Wille et al., 2024).

Melting of the Antarctic Ice Sheet is largely due to rising ocean and air temperatures, increased calving of icebergs, and the flow of warm water beneath ice shelves (Clem et al., 2023). However, snowfall has the potential to offset some of this melting. Snowfall is the primary input of surface mass balance (Palerme et al., 2017). As snow falls on the continent, it gains mass primarily in the center. This snowfall

eventually redistributes through wind and ice dynamics, contributing to the overall mass balance of the ice sheet. Snow predominantly falls along the coastal regions, however despite larger snowfall totals, these regions generally experience mass loss due to calving, basal melting, and surface melting (Rignot et al., 2011; Clem et al., 2023).

As the Earth warms, snowfall in Antarctica is predicted to increase due to the higher moisture-holding capacity of warmer air (Church et al., 2013). Increased snowfall is expected especially in interior regions of the continent where there is currently very little snowfall (Frieler et al., 2015). This increase can mitigate some of the effects of sea level rise from the melting AIS. In the past decades, increased snowfall has helped to offset some of the ice loss, although it is not enough to balance the accelerating ice discharge (Medley and Thomas, 2019).

There are still many unknowns when it comes to modeling how snowfall on the continent will change in the future, underscoring the importance of studying the current state of Antarctic snowfall. Current snowfall on the continent mainly occurs on the coasts, with less in the interior due to the cold, dry climate and the lower capacity of the air to hold moisture (Palerme et al., 2014). Coastal regions receive more snowfall due to the proximity to moisture sources and the influence of steep topography, which enhances precipitation (Palerme et al., 2014). The Antarctic Peninsula experiences higher snowfall rates due to its unique topographic and climatic conditions, which facilitate more frequent precipitation events (González Herrero et al., 2023). Elevations across the Antarctic Ice Sheet are presented in Fig. 1.1. From this map, it can be seen that the interior of the continent lies at a much higher elevation than the coasts. Furthermore, the EAIS has much higher elevation than the WAIS. This figure will be referenced throughout the paper as we discuss how elevation is related to snowfall on the AIS.

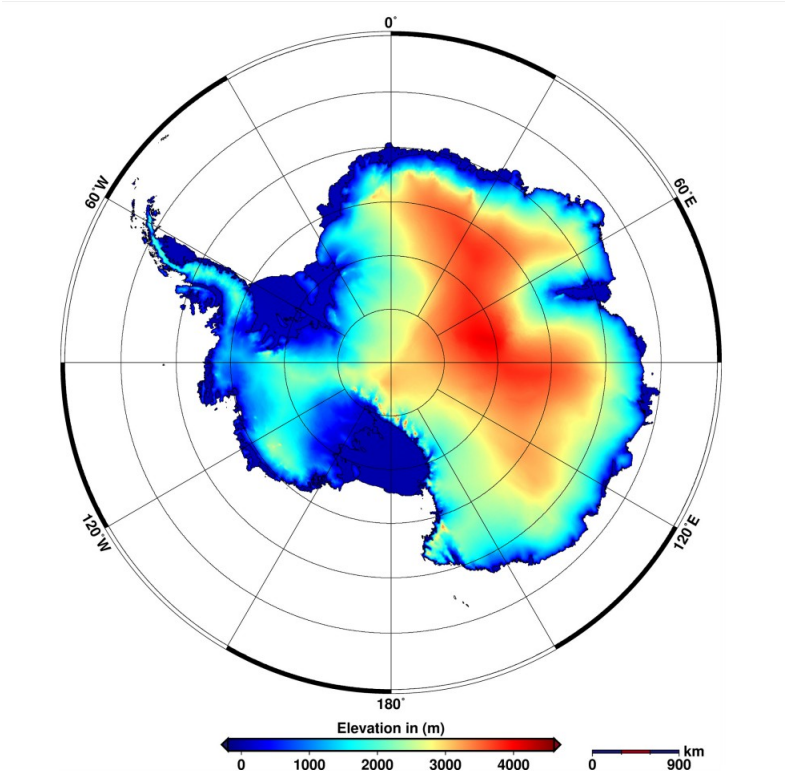

Figure 1.1: Elevation map of the Antarctic Ice Sheet derived from CryoSat-2 (Helm et al., 2014)

Extreme snowfall events, driven by atmospheric rivers, significantly contribute to annual snow accumulation in these regions. Atmospheric rivers are narrow bands of intense moisture transport from the ocean to the AIS, often leading to heavy snowfall when they interact with the continent's topography (Gimeno et al., 2014). Certain regions, like the Amery Ice Shelf and the Thwaites Glacier basin, experience frequent atmospheric river events, which are critical for understanding snowfall dynamics and their contribution to the ice mass (Turner et al., 2019; Maclennan et al., 2022).

Extreme snowfall events are essential for maintaining the mass balance of the AIS. From 2021-2022, the AIS showed record breaking mass gain of about 130 Gt/yr due to enhanced precipitation (Wang et al., 2023). In one region, two notably extreme precipitation events accounted for approximately 38% of the precipitation

anomalies during this time (Wang et al., 2023). Clearly, quantifying and studying the contributions of extreme events across the continent is essential for future projections of mass balance of the continent.

In a recent study, Rendfrey et al. (2024) use CloudSat snowfall retrievals to demonstrate that enhanced integrated vapor transport (IVT) events correspond to higher snowfall rates and frequency over both the Amery Ice Shelf of the EAIS and the Thwaites and Pine Island glacier basins of the WAIS. Their research highlights the significant role of moisture transport in driving snowfall processes across these regions. They found that during enhanced IVT events, the presence of an anomalous 850 hPa geopotential height pattern, characterized by a pair of low-pressure and high-pressure anomalies, facilitates moisture transport into the interior of the ice sheet, leading to increased snowfall rates.

Building on this foundation, this analysis takes a more general approach to understanding the source of extreme snowfall events on the AIS by characterizing moisture transport associated with all extreme snowfall events across the continent. As such, this study broadens the spatial scope of Rendfrey et al. (2024) by examining all Antarctic basins, rather than focusing on a select few. This comprehensive approach provides a more complete understanding of the relationship between moisture transport and snowfall across the entire Antarctic continent, highlighting the importance of extreme moisture transport events in shaping the surface mass balance of the ice sheet.

Due to its harsh conditions, in situ and ground-based observations of snowfall are rare in Antarctica. While ground-based instruments provide high temporal resolution, they are limited in spatial coverage and are susceptible to conditions like blowing snow (Grazioli et al., 2017). While some studies such as Gorodetskaya et al. (2014) have provided important initial evidence of links between isolated extreme

snowfall events and periods of anomalous water vapor transport, extrapolating these findings to the entire AIS requires satellite measurements. The launch of NASA's CloudSat in 2006 marked the first time spaceborne precipitation observations were available for the Antarctic ice sheet (Stephens and Ellis, 2008; Liu, 2008). Studies such as Palerme et al. (2014) have estimated annual snowfall rates across the AIS using algorithms developed from the CloudSat's Cloud Profiling Radar (CPR). However, CloudSat's snowfall estimates face a significant challenge. In the 1.2 km closest to the surface, radar side-lobes reflecting off the ground produce clutter that overpowers signals from hydrometeors in this region (Palerme et al., 2019). This creates a layer known as the blind zone in which the radar is unable to detect snowfall variations (Palerme et al., 2019). To address this issue, the CloudSat snow algorithm, 2C-SNOW-PROFILE (2C-SP), estimates surface snowfall from the 5th bin above the surface (Wood and L'Ecuyer, 2018).

This approach has its drawbacks, as snow can sublimate in this layer or shallow snow can form, which CloudSat will miss (Palerme et al., 2019). Antarctica is known for its strong and persistent dry wind, referred to as katabatic winds (Parish and Cassano, 2003). These winds are formed by a cold, thin layer of air that is cooled by radiation at the surface and then flows down the slope (Wendler et al., 1997). These winds occur across the whole continent, but are particularly common near the coasts where there is a steep drop off from the ice sheet (Wendler et al., 1997). Katabatic winds can sublimate snow as it is falling, referred to as virga, as these winds create a dry layer near the surface (Grazioli et al., 2017). The authors of Grazioli et al. (2017) used a ground based radar at Dumont d'Urville station on the Adelie coast and found that about 36% of snowfall detected was sublimated before it reached the surface, with a high correlation with the katabatic wind layer. They further estimated this effect across the continent with model data and found higher

ratios of sublimated snowfall along the coasts. Many of the effects of sublimation may be hidden from the CloudSat snowfall estimates.

To mitigate these problems, this study employs a unique dataset from another satellite. CloudSat is a part of NASA's A-train satellites, a group of satellites following similar orbital tracks (L'Ecuyer and Jiang, 2010). Another A-train satellite, the Cloud-Aerosol Lidar and Infrared Pathfinder Satellite Observation (CALIPSO), carries the Cloud-Aerosol Lidar with Orthogonal Polarization (CALIOP). Operating at a much shorter visible wavelength with a higher vertical and spatial resolution than the CPR, CALIOP is not subject to ground clutter at the surface (Winker et al., 2009). The complementary combination of CloudSat and CALIPSO measurements has been previously used to capture various cloud properties and radiative effects (L'Ecuyer et al., 2008; Sassen et al., 2008; Henderson et al., 2013; Mace and Zhang, 2014). This study will utilize a new dataset, the Combined CloudSat CALIPSO Snowfall (C3S), which uses CALIPSO snowfall estimates to improve issues with the CloudSat snow in the blind zone.

While satellite observations are essential for studying the AIS, there is still a need for ground based observations to accurately characterize surface conditions. Unlike satellite and reanalysis data, in situ measurements have a very high temporal resolution and do not rely on assumptions and measure relevant variables directly. Since 1980, the University of Wisconsin-Madison has managed a network of Automatic Weather Stations (AWS) through the Antarctic Meteorological Research and Data Center (AMRDC) (Lazzara et al., 2012). Today, the AMRDC has more than 60 AWS sites across the continent, which measure meteorological variables such as wind, temperature, and pressure (Lazzara et al., 2012). These data uniquely capture local conditions that would not otherwise be detected by satellite or models. This study will use AWS data to further explore meteorological conditions of extreme

snow from a ground-based perspective.

In this thesis, we aim to measure how much extreme snow is contributing to the ice mass of the Antarctic ice sheet, using the improved estimates of the C3S dataset. Furthermore, we aim to explore the atmospheric conditions that cause extreme snow and characterize how this differs across the continent. The next section will first expand on the C3S dataset and how it will be used in this study as well as supplemental datasets used to characterize snowfall cases. The following section will dive into two separate results. The first section of results will answer how much extreme snowfall is contributing to the mass of the AIS. The second section will answer what atmospheric conditions cause extreme snow and how this differs across the continent.

Chapter 2

Data and Methods

2.1 C3S dataset

The primary source of snowfall information used in this study were remotely-sensed snowfall intensity observations from CloudSat and CALIPSO. CloudSat carries the Cloud Profiling Radar (CPR), with a spatial resolution of 1.4 km (cross-track) by 1.8 km (along-track) (Tanelli et al., 2008). The CPR is a W-band radar, operating at 94 GHz which is sensitive to small hydrometeors such as ice particles and snow. CALIPSO carries the Cloud-Aerosol Lidar with Orthogonal Polarization (CALIOP) which has a spatial resolution of 333m by 30m (Winker et al., 2009). These two satellites take measurements from -82°S to 82°N, with one orbit taking 98 minutes and covering the entire earth every 16 days. The analysis spans from the end of 2006 to 2010, when CloudSat has the most complete day-night sampling (Milani and Wood, 2021). However, 2009 is missing months September through December due to an issue with CALIPSO. Data from November and December 2006 is used to supplement for this gap, although September and November only have three years worth of data. Although daytime-only observations are available for more than a

decade after this period, the lack of nighttime measurements precludes analysis of winter time snowfall events at the poles after early 2011.

For this study, a new product the Combined CloudSat CALIPSO Snow (C3S) is used for snowfall rates. This product is not yet published, but will be in the near future. C3S is based on the CloudSat 2C-SNOW-PROFILE (2C-SP) algorithm described in Wood and L'Ecuyer (2018), but modifies the product based on a CALIOP algorithm developed at l'École Polytechnique in order to improve snow rate estimates in the CloudSat blind zone. C3S takes each CloudSat footprint and uses a decision tree that we created in collaboration with the CALIPSO group at l'Ecole Polytechinque, described in greater detail below, to assess the snowfall estimate.

CALIPSO is a good candidate for reducing uncertainties of the 2C-SNOW-PROFILE missing snow in the blind zone. The CALIOP laser light provides direct sensitivity to backscatter from snow particles down to the surface with no ground clutter (Winker et al., 2009). These backscatter observations are related to surface snowfall rates through relationships developed from ground-based lidar and snowfall measurements at Summit Station, Greenland. However, the CALIPSO snowfall estimate is only valid when CALIOP is not fully attenuated.

C3S evaluates each CloudSat datapoint independently depending on the initial 2C-SP surface snowfall estimate. This value can either be a snowfall rate measured in millimeters per hour, no snow (a measurement of 0 mm/hr), or invalid snowfall. Additionally, the CloudSat 2C-SP evaluates the confidence of each snowfall estimate. For the C3S product, if the estimate is rated at "moderate" or "high" confidence, the value is referred to as a "good quality" CloudSat estimate. If an estimate is rated "no", "very low", or "low" confidence, the value is referred to as a "bad quality" CloudSat estimate. An independent surface snowfall estimate is then determined from CALIPSO observations for the corresponding CloudSat footprint. This value

can either determine no snow at the surface, give a snowfall estimate, or give an invalid value if the CALIPSO lidar is fully attenuated, meaning that the lidar is unable to take measurements near the surface.

As seen in table 2.1, C3S has six decision scenarios. If both the CloudSat algorithm and the CALIPSO algorithm do not detect snowfall at the surface, the C3S decision retains the original CloudSat decision of no snowfall. Likewise, when the CloudSat algorithm and the CALIPSO algorithm both detect snow at the surface, the CloudSat 2C-SP estimate is adopted as the snowfall rate at the surface. For this scenario, the CloudSat estimate must be good quality and CALIPSO lidar must not be fully attenuated. When the CALIPSO lidar is fully attenuated, the CloudSat 2C-SP decision is kept in the C3S decision, regardless of the CALIPSO surface detection since the lidar cannot detect surface snowfall. In contrast, when CloudSat snow is deemed bad quality, C3S takes the CALIPSO surface snowfall value regardless of the CloudSat snow value as long as CALIPSO is not fully attenuated.

Scenario	CloudSat Surface	CALIPSO Surface	CloudSat Quality	CALIPSO Fully Attenuated	C3S decision
Agreement - No Snow	No Snow	No Snow	Good	No	CloudSat
Agreement - Snow	Snow	Snow	Good	No	CloudSat
CALIPSO Fully Attenuated	Any	Any	Any	Yes	CloudSat
Bad Quality CloudSat	Any	Any	Bad	No	CALIPSO
Virga	Snow	No Snow	Good	No	CALIPSO
Shallow Snow	No Snow	Snow	Good	No	CALIPSO

Table 2.1: C3S decision tree

The two most important modifications of 2C-SP are captured in the last two

rows of table 2.1. When CloudSat detects snow at the surface but the CALIPSO algorithm does not, the C3S estimate determines that snow is not occurring at the surface. Snow that CloudSat detects in the 5th range bin above the ground is likely sublimating in the CloudSat blind zone, or virga is occurring in the lowest 1.2 km closest to the surface. Conversely, when CloudSat is unable to detect snow at the surface but CALIPSO does, the C3S algorithm uses the CALIPSO snowfall estimate. In this case, snowfall is likely developing in the lowest 1.2 km in the radar blind zone, causing it to go undetected by CloudSat. This will be referred to as shallow snow. Both of these final two scenarios require good quality CloudSat retrievals and CALIPSO is not fully attenuated.

2.1.1 Virga and Shallow Snow

An example of the last two scenarios is shown in Fig. 2.1. On the right, the CloudSat CPR reflectivity is shown. On the left, the CALIOP backscatter is shown. Both panels of the figure span the same satellite pathway as demonstrated by the corresponding latitude and longitude labels. The red box at the left of each panel highlights an area where the C3S algorithm has identified a case of virga. As seen by the high levels of reflectivity in the CPR at the height of the blind zone (1.2 km), the CloudSat 2C-SP algorithm has identified that there is snow in this region. However, when we look at the same region in the CALIOP backscatter, the dark blue values indicate that there is no snowfall at the surface. This implies that the snowfall detected at the top of the blind zone was sublimated within the lowest layer.

The blue box in the center of each panel highlights an area where shallow snow was identified by the C3S algorithm. Looking at the CloudSat CPR, the top of the box has very low values of reflectivity, which the 2C-SP algorithm identifies as no

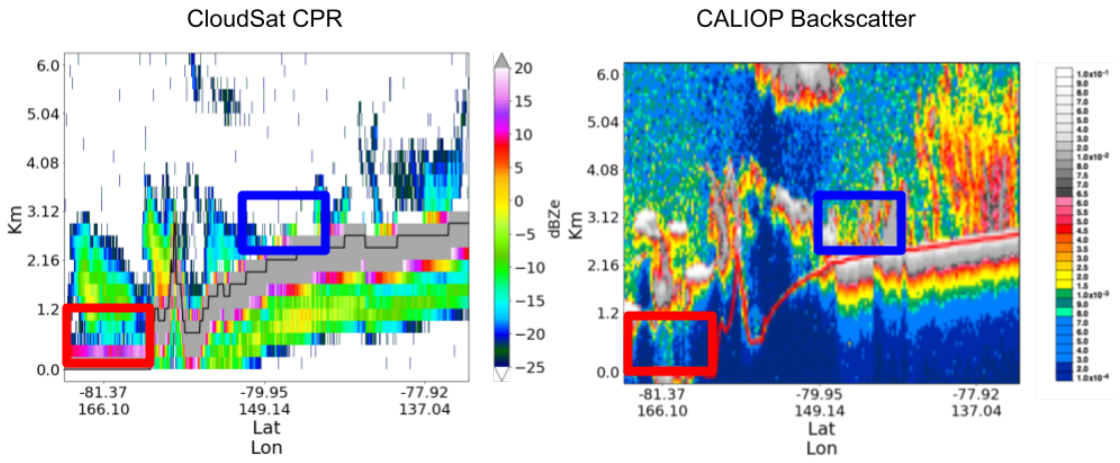

Figure 2.1: An example of virga (red box) and shallow snow (blue box). Each panel shows the along track path on the x-axis and the 0 to 6 km vertical of the y-axis. The left panel shows the CloudSat CPR reflectivity (dBZe) and the right panel shows the CALIOP backscatter ($km^{-1}sr^{-1}$).)

snow. On the other hand, the CALIOP panel shows higher values of backscatter near the surface. The C3S algorithm identifies this as shallow snow, indicating that that snowfall has formed in the blind zone layer, undetected by CloudSat.

Now that we have explored how the C3S algorithm identities such cases, we can look at how often this occurs over the AIS. Fig. 2.2 shows the frequency of virga on the left and shallow snow on the right over the AIS and surrounding southern ocean. Of all C3S datapoints, the frequency of both of these scenarios is detected between 0 and 15% of the time. The frequency of virga is highest in east Antarctica near the coasts. There is much less frequency over the interior of east Antarctica. In contrast, in west Antarctica, virga frequency is highest in the interior. These patterns may be due to katabatic winds. Katabatic winds have been shown to aid in the sublimation of snowfall near the surface (Grazioli et al., 2017). These winds

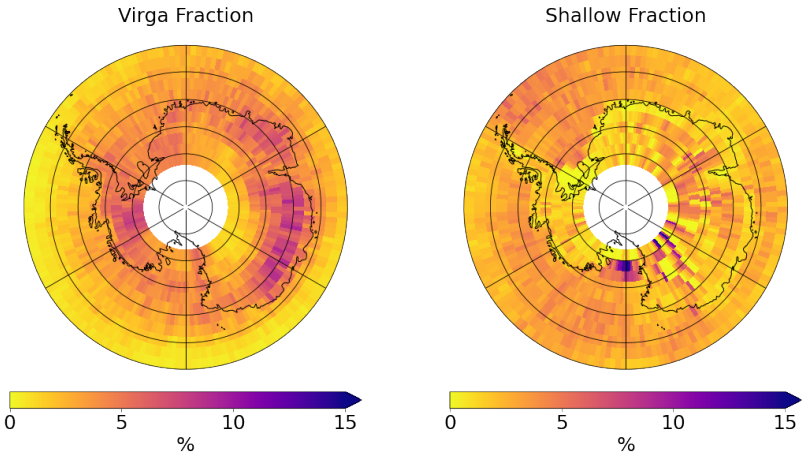

Figure 2.2: Virga frequency (left), shallow snow frequency (right)

are especially prevalent in eastern Antarctica near the coast, similarly to where the virga frequency is higher (Grazioli et al., 2017).

The shallow snow frequency presents an interesting pattern of high frequency occurrences appearing in bands especially in east Antarctica. These bands of high frequency shallow snow correspond well to changes in topography of the ice sheet. Regions that have higher rates of shallow snow frequency, especially in East Antarctica, are consistent with elevation changes seen in Fig. 1.1. Specifically, shallow snow is occurring where there is a steep gradient in topography.

Finally, the frequency (left) and annual accumulations (right) of snowfall from the whole C3S dataset are shown in Fig. 2.3. From the frequency of snowfall plot, we can see that snowfall is more frequently observed over the southern ocean and the coastal regions of the continent, with frequencies reaching nearly 50% in some regions. Conversely, the interior of the AIS sees very low snowfall frequency. There is a contrast between East and West Antarctica, with the interior of west Antarctica receiving more frequent snowfall than east. In East Antarctica the patterns seen

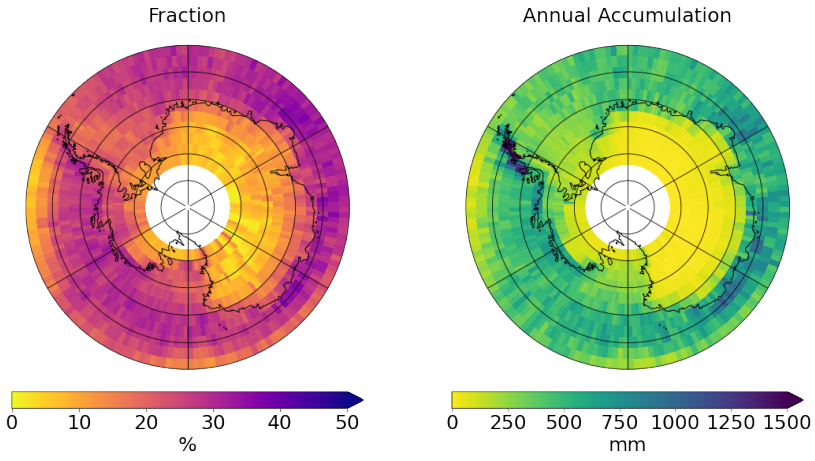

Figure 2.3: C3S climatology: Frequency of snowfall detected by C3S (left), Mean Annual Accumulation (right) from 2006-2010

in the shallow snow plot are still able to be seen. This gives us insight that the shallow snow modifications made from CALIPSO observations have an impact on our dataset. However, these patterns have a much lesser impact on the annual accumulation as seen in the right panel of the figure. From this figure, we can also see that annual snowfall accumulations are greater in coastal regions and much lower in the interior of the continent. This annual accumulation result is similar to that found in Palerme et al. (2014), however the subtle changes in the fraction of accumulation specific to the C3S product will be essential to this analysis.

2.1.2 Additional quality control

While the C3S algorithm improves CloudSat estimates from the blind zone, some issues persist. Specifically, the 2C-SP algorithm struggles with steeply varying terrain due to excess ground clutter. In such cases, using the 5th bin above the surface may not suffice to eliminate surface clutter (Wood and L'Ecuyer, 2018). Addition-

ally, incorrect surface elevation assumptions can lead to the wrong bin being used to calculate surface snow. For more general precipitation studies, these issues have minimal impact. However, the focus of extreme events in this study necessitates special attention to these cases as they often record unusually high snowfall rates.

We constructed the following methods in order to vet these cases with extreme precision. The CloudSat 2C-SP has a flag used to identify possible issues such as those described above. This flag is registered where the snowfall rate at the base of the snowfall layer is substantially larger than in the profile bin immediately above (Wood and L'Ecuyer, 2018). If the C3S product had not already replaced a snowfall estimate where this flag was triggered, the data was replaced with CALIPSO snow if the CALIPSO lidar was not fully attenuated. If the CALIPSO lidar was fully attenuated, the snowfall rate was not used in the dataset.

Despite the initial filter, some problematic cases remained. Often, the 2nd bin from the surface was also affected by surface clutter, failing to trigger the filter. Through repeated trials, we determined that the ratio between the surface bin and the 4th bin above the surface was an effective metric for identifying these cases. Cases with a ratio greater than 50 indicated an unrealistically large gradient than could not be supported by shallow snow microphysics. These cases were either replaced with CALIPSO snowfall estimates or removed from the dataset.

The DEM elevation used in the CloudSat 2C-SP product is sometimes inaccurate, especially around coastal regions in Antarctica, leading to extreme overestimates in snowfall. An example of this issue is illustrated in Fig. 2.4. In this figure, the CloudSat CPR reflectivity values are shown along with two surface lines: the upper red line (solid) indicates the actual surface, while the lower red line (dotted) represents the DEM surface data. In cases such as these, high reflectivity values due to ground clutter are sometimes misclassified as high snowfall rates. To correct this,

we used the 2B-GEOPROF product to identify the vertical reflectivity for each snow profile. The bin with the maximum reflectivity was identified as the actual surface, as it produces a much higher reflectivity value than the snow measured in our dataset (Palerme et al., 2017). This correction is evident in Fig. 2.4, where the actual surface line corresponds to reflectivity values exceeding 25 dBZe, shown in gray on the colorbar. Cases where the difference between the maximum reflectivity bin and the surface height bin where greater or equal to two were flagged as problematic. This data was then replaced with CALIPSO if the lidar was not fully attenuated or taken out of the dataset.

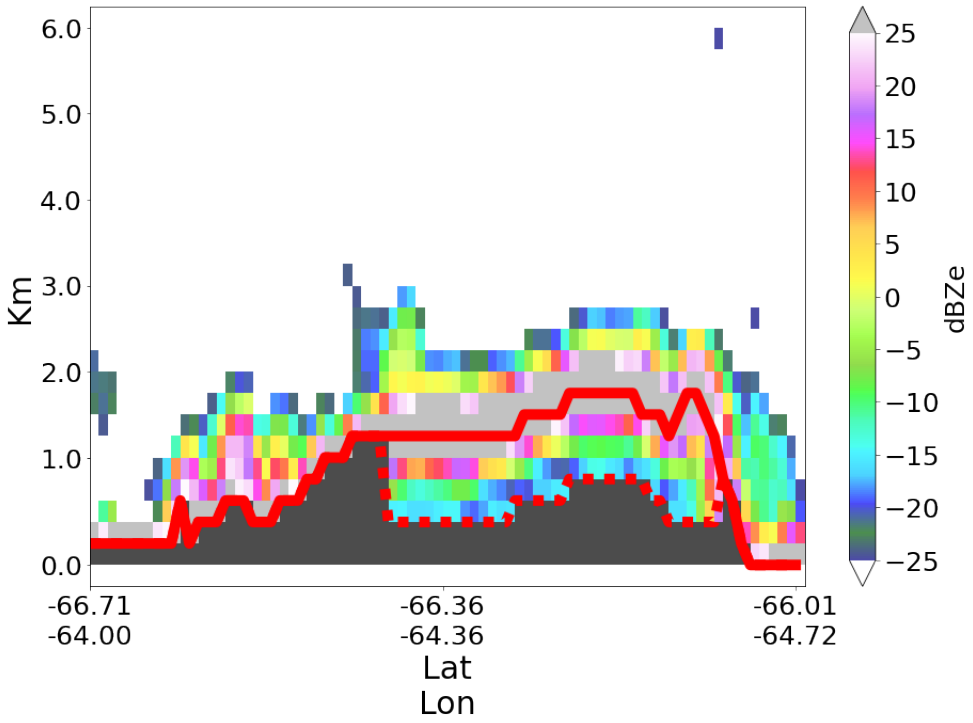

Figure 2.4: As in Fig. 2.1a, but for a case where the DEM is inaccurate. The red line represents the surface, with the top line (solid) representing the actual surface and the bottom line (dotted) representing the incorrect DEM.

While these additional quality control methods are time-consuming, it was important to make sure that higher snowfall rates were properly identified in order to measure the impact of extreme snow.

2.1.3 Remaining Uncertainties

Even with the addition of CALIPSO lidar data and additional quality control, the C3S dataset may not capture all snow correctly due to uncertainties inherent in radar and lidar retrievals. While C3S snowfall estimates have yet to be evaluated with ground based radar estimates, a number of studies have done so for the 2C-SP product. Instantaneous snowfall estimates generally exhibit uncertainties of a factor of two or more for individual CloudSat fields of view (Wood and L'Ecuyer, 2021), but these errors have a large random component that often decreases substantially when averaged over thousands of samples (Palerme et al., 2017). However, some studies indicate that the 2C-SP product may underestimate heavy, wet snowfall (Cao et al., 2014; Norin et al., 2015; Chen et al., 2016). Specifically, these studies concluded that 2C-SP underestimates snowfall over 1 mm/hr, possibly due to attenuation of the signal. However, studies that evaluated the 2C-SP product specifically over the Antarctic ice sheet found that snowfall had good agreement with snowfall climatology near micro-rain radar observations (Souverijns et al., 2018; Lemonnier et al., 2019). This is consistent with the fact that snowfall rates are generally much lighter over the AIS than in the regions analyzed in the midlatitudes (Mroz et al., 2021). Even the extreme Antarctic snowfall events analyzed in this study tend to be light when compared with global snowfall and rarely exceed 1 mm/hr as we find below. One exception is the Antarctic Peninsula where we find extreme snow rates to exceed this threshold more often, the results from this region should be taken with some caution.

While C3S provides a clearer picture of snowfall in the lower atmosphere, the CALIPSO observations in the three lowest layers introduce another source of uncertainty that was not previously an issue in the 2C-SP product. Because of Antarctica's strong, persistent winds, blowing snow is a frequent occurrence across the

continent (Palm et al., 2017). Since studies such as Palm et al. (2011, 2017) have shown that CALIOP can be used to detect these types of events, it is logical to conclude that the CALIPSO estimates of falling snow may be influenced by blowing snow.

2.2 Defining Extremes

The methods found in this section of the paper are based on those found in Pendergrass and Knutti (2018). In this paper, the authors sought to measure the variability in global rainfall distribution, highlighting that heavy rainfall events contribute disproportionately to annual rainfall. More specifically, they wanted to answer the following question, what fraction of total rain occurs beyond the top p percentile of days in a period? They found that rain events from greater than the ninety-fifth percentile account for over half of the global rainfall. Following these results, we examine what fraction the ninety-fifth percentile of intense snowfall events contribute to total Antarctic snowfall. The ninety-fifth percentile snow was therefore chosen as the threshold for extreme snow in this study. Like Pendergrass and Knutti, we also answer the question of what snowfall intensity percentile accounts for half of precipitation accumulation on the AIS.

In order to find the 95th percentile snow, a cumulative distribution function (CDF) was created from all C3S instantaneous snow rates over the Antarctic continent. From the CDF, the 95th percentile snow rate was determined. Fig. 2.5a demonstrates the CDF curve for the whole Antarctic continent, with snow rates on the x-axis and the cumulative percentile on the y-axis. Furthermore, the figure demonstrates the 95th percentile with a horizontal line and the corresponding snow rate with a vertical line.

To calculate the fraction of accumulation from extreme snow, a cumulative accumulation was computed. First, the mean snow rate is determined as the average of all instantaneous snow rates, as shown in equation 2.1. Next, the annual accumulation is calculated by multiplying the mean snow rate by the number of hours in a year, as described in equation 2.2. Once the total annual accumulation is established, the annual accumulation for all snow rates less than a given snow rate X is computed. Specifically, for a given snow rate X, the accumulation from snow rates less than X is defined as the mean snow rate for snow rates below X, multiplied by the number of hours in a year, as shown in equation 2.3. When this is repeated for all snow rates of X, the resulting function is a continuous cumulative accumulation that indicates the accumulation contributed by snowfall with rates up to any specified value.

$$\begin{gathered}\text{mean snow (mm/hr)} \\ = \text{average of all instantaneous snow rates in Antarctica (mm/hr)}\end{gathered} \tag{2.1}$$

$$\begin{gathered}\text{annual accumulation (mm/yr)} \\ = \text{mean snow (mm/hr) x \# of hours in a year (hr/yr)}\end{gathered} \tag{2.2}$$

$$\begin{gathered}\text{annual accumulation (snow rates } < X) \\ = \text{mean snow (snow rates } < X) \text{ x \# hours in a year}\end{gathered} \tag{2.3}$$

Finally, if each cumulative accumulation is divided by the total accumulation, the resulting function is a cumulative percent of the accumulation, shown in Fig. 2.5b. Like Fig. 2.5a, the x-axis shows snow rates, however the y-axis represents the percent of the total accumulation. For a given X, the curve shows the percent of

accumulation from snow rates less than X. This function will be called a weighted CDF because the cumulative sum is weighted by the accumulation of each snow rate.

Once the CDF and weighted CDF are calculated, the fraction of accumulation due to extreme snow can be found. Using the 95th percentile snow rate found earlier, the corresponding weighted percentile can be found. Fig. 2.5c demonstrates the final step in this process. Both the CDF (red curve) and the weighted CDF (blue curve) are overlaid in this figure. In addition to the 95th percentile and corresponding snow rate, the second horizontal line represents the corresponding percent of accumulation. This fraction must be subtracted from 100 since the weighted percentile is defined as the percent of accumulation less than X. This number represents the percent of accumulation that comes from the top 5 percent highest snow rates on Antarctica.

Alternatively, in order to calculate the percentile that accounts for half of the accumulation, first the 50 percent accumulation snow rate must be calculated from the weighted CDF. Once this snow rate is found, the unweighted CDF value is calculated for the same snow rate. This value gives us the percentile for which half of the accumulation comes from. In other words, snow rates greater than this percentile makeup half the snow accumulation on Antarctica.

2.3 Drainage Basins

In order to understand variations in the contributions of extreme events and the conditions that cause them across the AIS, we divided the AIS by basin. Therefore, in addition to performing this analysis on the Antarctic continent as a whole, we repeated the analysis on Antarctic drainage basins defined by Zwally et al. (2012)

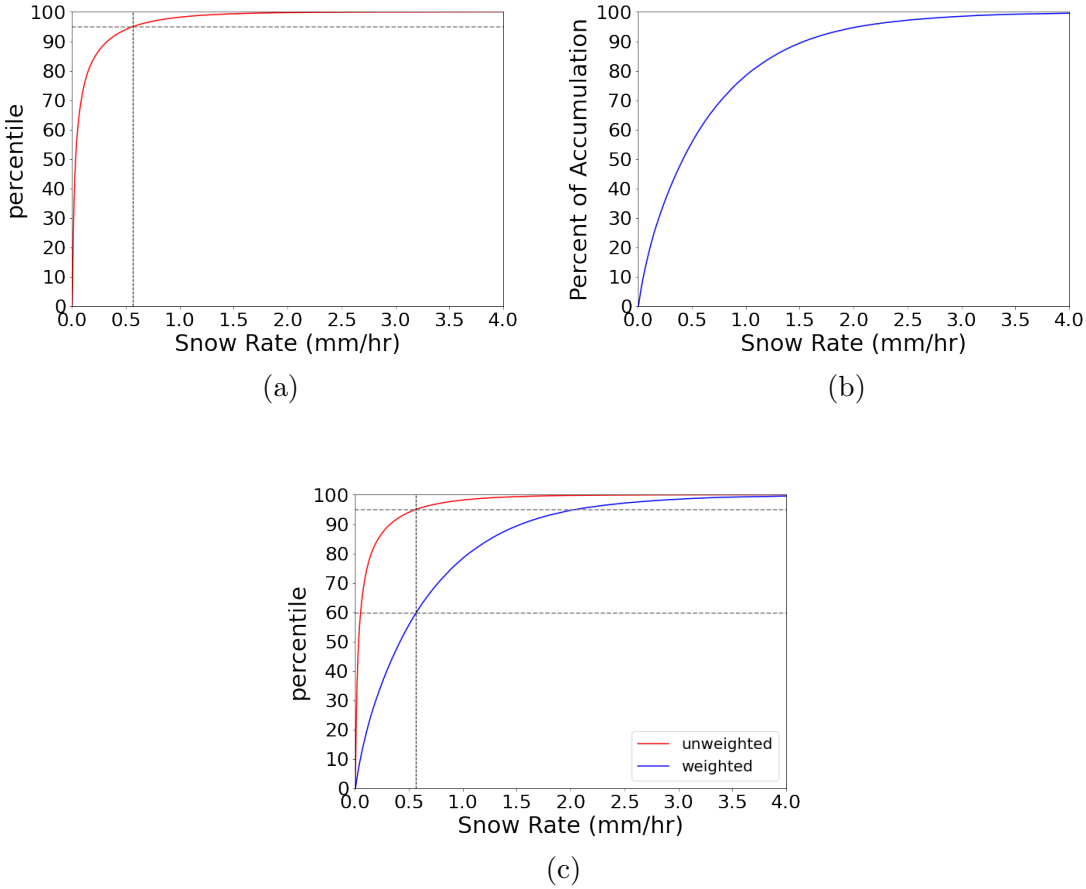

Figure 2.5: Antarctic CDF (a), weighted CDF (b), total process (c)

shown in Fig 2.6. These basins have a consistent surface slope relative to atmospheric advection (Zwally et al., 2012). Ice mass balance can be considered for each individual basin, which is relevant to this analysis.

The number of C3S snowfall data points for each basin is shown in table 2.2. The first row shows the number of C3S extreme snowfall counts in each basin. To avoid counting the same storm multiple times when establishing the synoptic conditions that favor extreme snowfall events, the second row shows the number of C3S extreme snow counts when data repeated in the same CloudSat orbit is removed. The details of how this second value are used are described in the reanalysis section below. This table shows that while the number of extreme snowfall cases differs between basins,

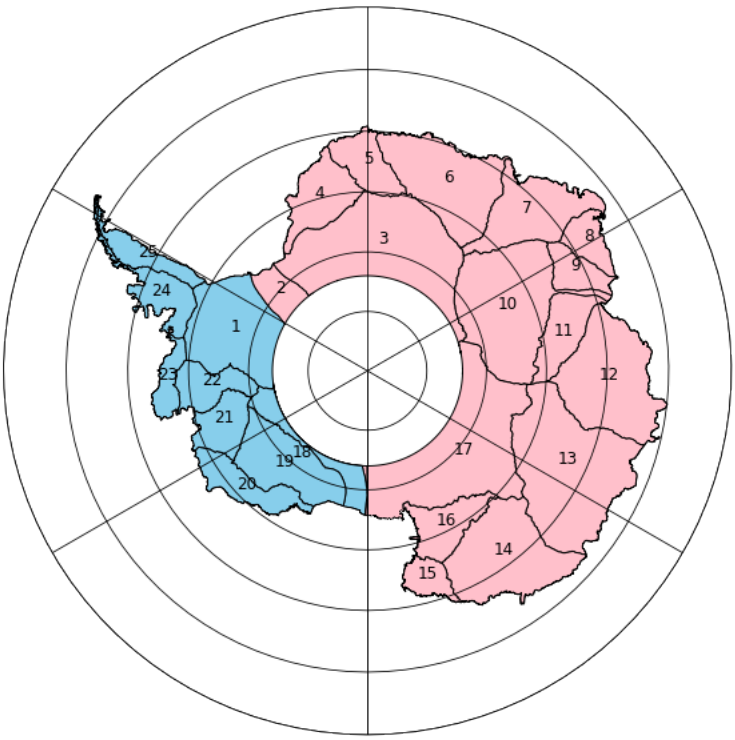

Figure 2.6: Drainage basins for the AIS. Basins located in the WAIS are shown in blue while basins located in the EAIS are shown in pink.

all basins contain at least 60 cases, with many greatly exceeding that number.

2.4 Reanalysis

To understand the atmospheric conditions associated with extreme snowfall for the Antarctic drainage basins, we examined sea level pressure, total precipitable water vapor, and surface wind vectors from reanalyses. NASA's Modern-Era Retrospective analysis for Research and Application (MERRA-2) provides an hourly gridded reanalysis product with a horizontal resolution of 0.625 $\times$ 0.5 and 72 levels in the

Basin	1	2	3	4	5	6	7	8	9
C3S	28334	6827	25216	7644	3885	9478	6399	2109	2213
Unique C3S	904	213	844	244	109	283	227	82	66
Basin	10	11	12	13	14	15	16	17	18
C3S	11917	2763	11703	12674	8632	1987	2673	29889	12417
Unique C3S	668	90	349	370	277	86	145	1052	534
Basin	19	20	21	22	23	24	25		
C3S	15115	10474	9518	8138	4590	7100	3646		
Unique C3S	603	443	301	284	242	396	194		

Table 2.2: Number of C3S extreme snow counts for each basin, as well as the number of C3S extreme snow counts from unique overpasses

vertical (Gelaro et al., 2017). The MERRA-2 dataset spans from 1980 to present, however only months matching the C3S dataset (November 2006 - December 2010) were used in this analysis. The variables used were sea level pressure, surface wind speed, and total precipitable water vapor.

Times identified as extreme snow from the C3S dataset were co-located with the nearest time from the MERRA-2 reanalysis. Since CloudSat and CALIPSO take multiple data points in a single overpass of the continent, only one time was taken per granuale as to not have repeating MERRA-2 data. Composites were taken from the departure from monthly averages, so as to detrend the data from any seasonal biases. Finally, a two-tailed t-test at the 99% confidence level was performed to identify regions of significance in the composites.

2.5 Automatic Weather Stations

As an independent verification of the principle findings in this study, data from the Antarctic Meteorological Data and Research Center's (AMRDC) Automatic Weather Station (AWS) network were used to examine conditions at the ground during satellite-detected extreme snowfall events. This data contains 10 minute

observations of temperature, pressure, wind speed, and wind direction. For this analysis, Mizuho AWS and Linda AWS data were used (AMRDC, 2022). The location of these two stations is shown in Fig. 2.7 along with all AWS managed by the AMRDC. The locations of Linda and Mizuho are marked with a star. These stations were used because of the largely continuous data in the time period of interest and the contrasting conditions of these two AWS. As seen from the figure, Mizuho and Linda lie on opposite sides of the continent. Furthermore, Mizuho AWS sits at a much higher elevation of 2260 meters whereas Linda AWS is only 46 meters above sea level. These vastly different locations will give us insight into how conditions vary in these region.

To analyze extreme snow conditions at these stations, AWS data were matched with the times identified as extreme snow events by C3S. Extreme snow cases were selected from the basin in which each AWS station is located: Mizuho AWS in basin 7 and Linda AWS in basin 17. Similar to the MERRA-2 analysis, only one time point per granule was chosen to avoid duplicate data. Anomalies were calculated as deviations from the monthly averages to remove any seasonal biases from the data.

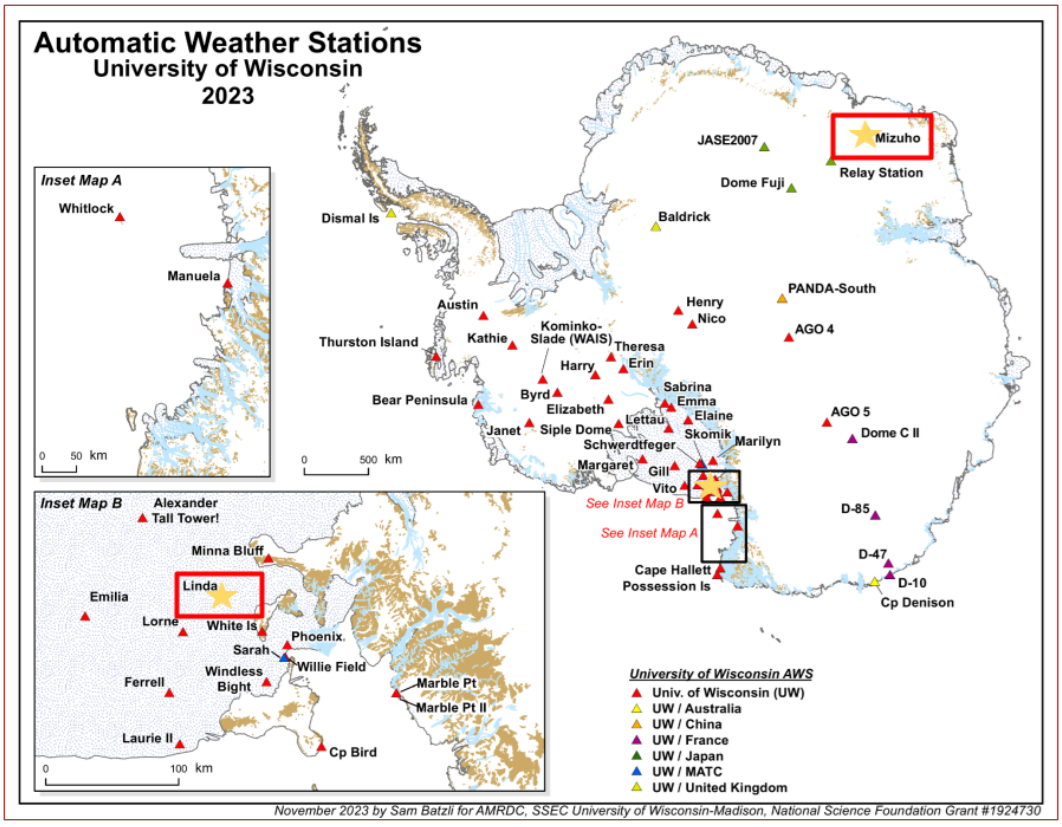

Figure 2.7: Location of all AWS associated with UW-Madison's AMRDC as of 2023 (AMRDC, 2022).

Chapter 3

Results

3.1 How much do extreme snow events contribute to the ice mass of the Antarctic Ice Sheet?

In this section, we present the findings on the distribution and impact of extreme snowfall rates across the Antarctic Ice Sheet. We begin with a continental overview, followed by a detailed analysis of individual drainage basins, and conclude by examining contributions to ice mass balance. This analysis provides insights into the spacial variability of extreme snow and their significance in the context of Antarctic ice mass accumulation.

3.1.1 The whole AIS

Using the process shown in Fig. 2.5, extreme snow rates were found for the whole continent. The 95th percentile snow rate for all of Antarctica was found to be 0.57 mm/hr. From Fig 2.5, the fraction of accumulation from extreme snow was found to be 40.3%. In other words, the top 5% most extreme snow events account for 40.3% of the annual accumulation for the whole continent.

Following the methods of Pendergrass and Knutti (2018), the snowfall rate responsible for half of the accumulation on the whole continent was found to be 0.42 mm/hr and higher. This snowfall rate corresponds to the 92.5th percentile snow so, half the accumulation on the continent originates from the top 7.5% most extreme events. While this is lower than the global precipitation found in Pendergrass and Knutti (2018), the authors did find some regions fell below the 50% accumulation mark, such as the tropical western pacific.

3.1.2 Basin Analysis

To determine how this result varies across distinct regions of the AIS, this analysis was then repeated for each drainage basin using the same process as Fig. 2.5. Extreme snow is calculated as the top 5% of the total snowfall in each basin. For context, the location of extreme snow events found in each basin are plotted in Fig. 3.1. The location of each recorded extreme snow rate is plotted with a dot corresponding to that basin's unique color. While the number of extreme rates differs between basins, each basin still contains 5% of its respective snowfall rates. This results in the number of extremes being scaled by differences in the number of events.

A stark contrast can be seen in basins that lie on the EAIS and the WAIS. On the EAIS, extreme snowfall rates are primarily found near the coastal regions. The interior of these basins is largely void of any extreme snow rates, with the exception of basin 10. The location of extremes in basin 10 is anomalous due to its unique shape that contains very little coastal area compared to other basins. In contrast, for basins in the WAIS, extreme snowfall rates are found throughout the basin, with no discernible preference for the coast or other region.

Compared to the topography map shown in Fig. 1.1, this difference may be

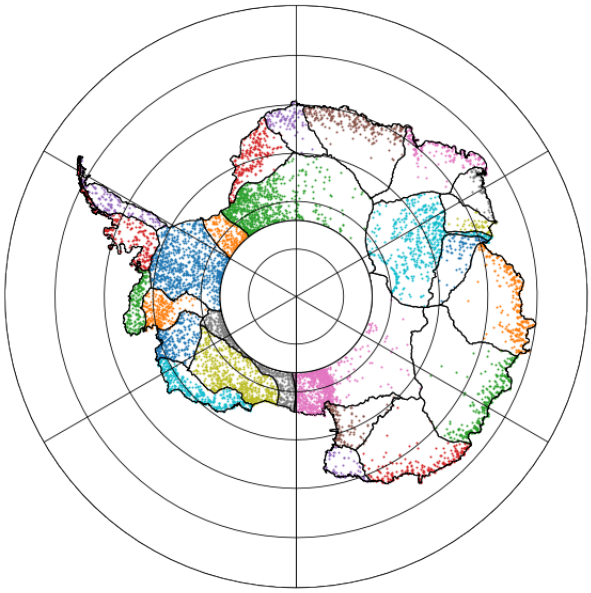

Figure 3.1: Locations of extreme snowfall detected by C3S. Basin outlines can be seen in black, additionally each basin is assigned a unique color to show extreme locations.

explained by the difference in topography found in the two regions. Eastern Antarctica is characterized by higher elevation and steeper elevation slopes that make it difficult for moisture to reach the interior. Western Antarctica does not contain as high of elevation, with more gradual slopes, which are more favorable for interior snowfall events.

The extreme snow rate (left) and the fraction of accumulation from extreme snow (right) for each basin are shown in Fig. 3.2. The extreme snow rate thresholds range from 0.1 mm/hr to 1.2 mm/hr. These extreme snow rates are still very modest when compared to snow in the midlatitudes. This further confirms that CloudSat's bias for heavy snow discussed in section 2.1.3 is of minimal concern for this most basins in this analysis. It can be seen that extreme snow rates are greater in more

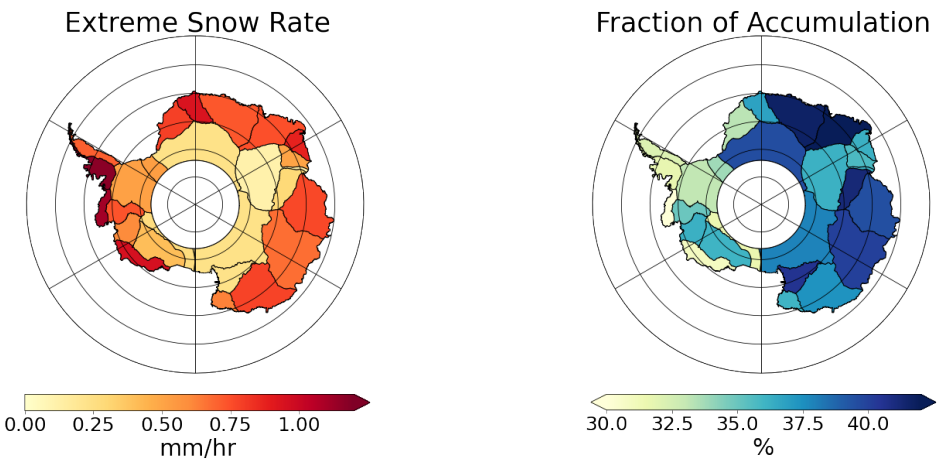

Figure 3.2: Extreme snow rate threshold (left) and fraction of accumulation from extreme snow (right)

coastal basins, whereas basins with little coastal area exhibit much lower extreme snow rates. These interior basins have a higher elevation, which hinders moisture intrusions, leading to lesser snow rates even for the most extreme events. The considerable variation in extreme snow rates between basins highlights the necessity for each basin to define extreme snow individually, reflecting their distinct snowfall patterns and amounts.

The fraction of accumulation from extreme snow ranges from 30% to 42%. Eastern Antarctic basins generally exhibit higher fractions of accumulation from extreme snow, often exceeding the 40.3% threshold observed for the entire continent. Conversely, many basins in West Antarctica show a lower fraction, often less than 32%. Notably, a higher extreme snow rate does not necessarily correlate with a higher fraction of total accumulation from extreme snow. For instance, the West Antarctic Peninsula basin (basin 24) has the highest extreme snow rate of 1.2 mm/hr, yet these rates contribute only 32% to the total accumulation. This is likely due to the

peninsula's geography, which favors high snowfall rates in general, thus reducing the relative impact of the top 5% most extreme events. In contrast, basin 16, located to the east of the Ross Ice Shelf, has a much lower extreme snow rate of 0.25 mm/hr, but this accounts for nearly 40% of the accumulation. This significant contribution is because most snowfall rates in this basin are very low, making any higher snowfall rates critically important to the total accumulation. This contrast highlights the differing snowfall distributions and climatological conditions between the basins.

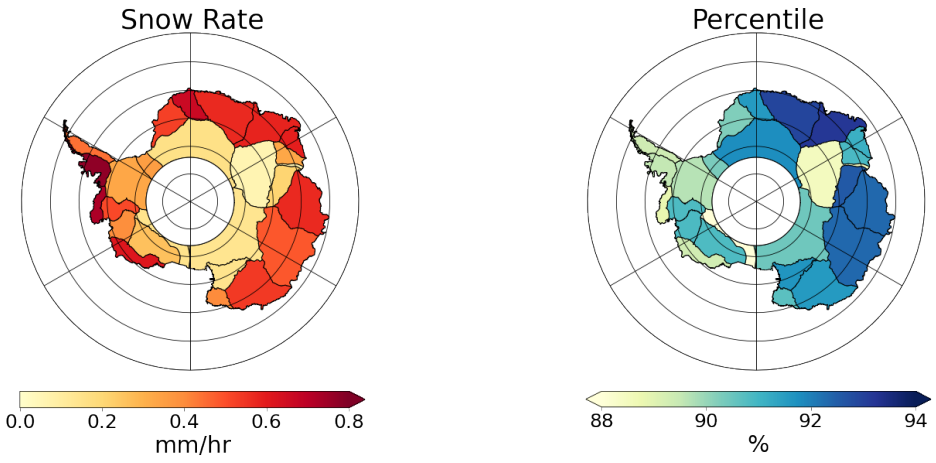

Figure 3.3: Snow rate corresponding to half the accumulation (left) and percentile accounting for half the accumulation (right)

Building on the approach of Pendergrass and Knutti (2018), it is instructive to compare the percentile and corresponding snow rates that account for half of the accumulation in each basin (Fig. 3.3). The snow rates accounting for half of the accumulation in each basin exhibit a wide range from 0.06 mm/hr to 0.77 mm/hr. Similarly to the previous figure, snow rates are higher in more coastal basins and lower in more interior basins. While intensities vary widely, the percentile accounting for half the accumulation only ranges from the 88th percentile to the 93rd percentile.

So while no basin's percentile reaches the 95th percentile, as was found by Pendergrass and Knutti (2018) for global rainfall, some basins get close. Furthermore, this highlights how some more moderate events, below what we define as extreme, are still important for accumulation totals. As is the case for the 95th percentile, higher snow rates do not correlate with a higher or lower percentile accounting for half of the accumulation. Unlike the previous figure, higher percentiles do not necessarily favor East Antarctica and do not appear to be characterized by a particular pattern.

3.1.3 Ice Mass

While accumulation is an important metric for measuring the contribution of extreme snow rates, when describing the contributions to ice mass balance of the continent, snow mass contribution may provide a more useful metric for comparing to mass balance models. In Fig. 3.4, the total mass from snowfall in Gigatons per year is plotted on the left alongside the mass from just extreme snow on the right. The total mass from snowfall for the continent is 1318 Gigatons per year, this is comparable to other estimates by CloudSat and models (Palerme et al., 2014; Clem et al., 2023). Two factors contribute to the snow mass of individual basins: their mean snow rate and their area. Thus basins with high snowfall rates and/or large basins with moderate snowfall rates have the largest contributions to the annual mass gain of the ice sheet. Looking at the mass from just extreme snow tells a similar story. Basins with higher extreme snow rates and greater surface areas have the greatest snow mass gain from extreme snow. Extreme snow can contribute up to 52 gigatons per year in a single basin, such as basins 12, 13, and 14 in East Antarctica. Extreme snow contributes 476 gigatons per year from all basins which is about 36% of the total snow mass contributions for the whole continent. This again highlights the importance of extreme snowfall for the continent especially in

regards to ice mass balance.

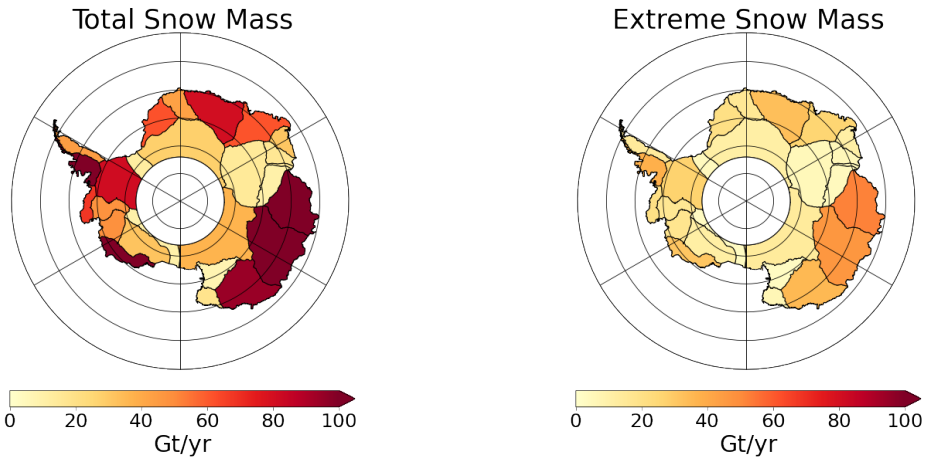

Figure 3.4: Total snow mass (left) and mass from extreme snow (right)

3.2 What atmospheric conditions cause extreme snow and how does this differ across the continent?

To infer how the distribution of snowfall intensity and the contribution of extremes might change in a warmer climate, it important to understand the synoptic conditions that promote extreme snowfall events in Antarctica. For this purpose, we examined sea level pressure (SLP) anomalies, total precipitable water vapor (TPWV) anomalies, and local Automatic Weather Station (AWS) observations associated with the 95th percentile snow events identified in section 3.1. By analyzing these variables during times of extreme snowfall, we aim to identify the atmospheric patterns and moisture transport mechanisms contributing to these extreme events. This

section details the findings from SLP anomalies, TPWV anomalies, and AWS analysis, providing a comprehensive view of the atmospheric conditions during extreme snowfall.

3.2.1 Sea Level Pressure Analysis

In order to show synoptic conditions during extreme snowfall, sea level pressure anomalies were plotted during times experiencing extremes for each basin. Extreme snowfall is defined the same as in the previous section, snow rates greater than the 95th percentile.

In Fig. 3.5, sea level pressure anomalies during extreme snow cases are shown for all 25 basins. Positive anomalies are shown in red and negative anomalies are shown in blue. Many basins exhibit a sea level pressure dipole, with a low pressure anomaly to the west of the basin (highlighted in yellow) and a high pressure anomaly to the east of the basin. The basins can be divided into three sea level pressure anomaly regimes, strong dipole, weak dipole, and no significant dipole. These three regimes were found from calculating the difference between the maximum sea level pressure anomaly and the minimum sea level pressure anomaly from each basin. The regimes were defined from natural clusters that could be found in the data. This is demonstrated in 3.6, where the values of the SLP difference are plotted for each basin and the vertical lines show the cut offs for each regime.

The strong dipole regime is defined as basins with a difference between high and low pressure anomalies greater than 15 hPa. Eleven of twenty five basins exhibit this strong dipole regime for extreme cases. An example of a strong dipole regime basin is shown in Fig. 3.7. In addition to the sea level pressure anomalies shown in the previous figure, this figure also contains wind vector anomalies and shading to indicate regions of significance. In this example, the low pressure anomaly is present

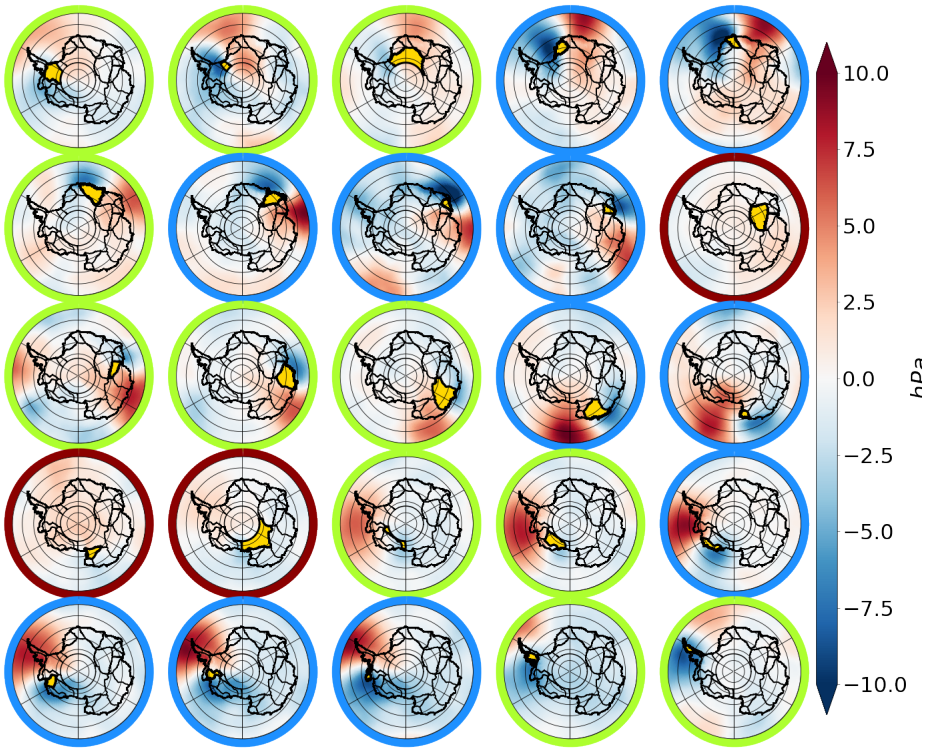

Figure 3.5: SLP anomalies coinciding with extreme cases. Basins circled in blue experience the strong SLP dipole regime, basins in green experience the weak SLP dipole regime, and basins in red do not experience a significant SLP dipole.

to the west of the basin and the high pressure anomaly is found to the east. The shading shows that both of these regions are statistically significant. The surface wind anomalies show northerly wind anomalies in between the high and low pressure systems. These winds point from the ocean towards the basin shown, which would be expected to bring warmer, moist air to the continent.

The weak dipole regime is defined as basins with a difference between high and low pressure anomalies between 8 hPa and 15 hPa. Another eleven of twenty five basins exhibit a weak dipole regime during extreme cases. An example of a weak

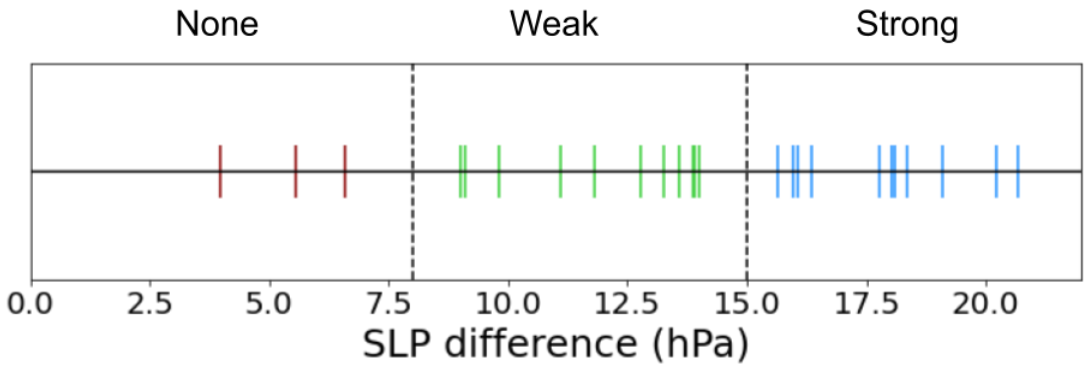

Figure 3.6: Difference between maximum and minimum SLP anomalies for each basin. Each basin's SLP difference is represented by a mark on the number line in order to demostrate the natural clusters in the data. The horizontal lines represent the thresholds separating the three regimes, no dipole present (red), weak dipole (green), and strong dipole (blue).

dipole regime basin is shown in Fig. 3.8. This figure shows sea level pressure anomalies, surface wind anomalies, and has statistically significant regions shaded. Like in the strong dipole regime, a low pressure anomaly is found to the west and a high pressure anomaly is found to the east. However, the low and high pressures have a lesser magnitude than in the strong dipole cases. The northerly wind anomalies are still present, which would still be expected to bring warmer moist air to the continent.

In the third and final regime, no significant dipole is observed. Only three basins exhibit this regime. An example of a basin with no significant dipole is shown in Fig. 3.9, with sea level pressure anomalies, surface wind direction anomalies, and statistically significant regions again shown like the previous two figures. This example shows very weak anomalies across the continent. The dipole pattern found in the previous two regimes does not appear to be present. The regions that are statistically significant support that this case does not have a dipole pattern. Lastly, wind anomalies do not appear to show a northerly wind pattern near the basin

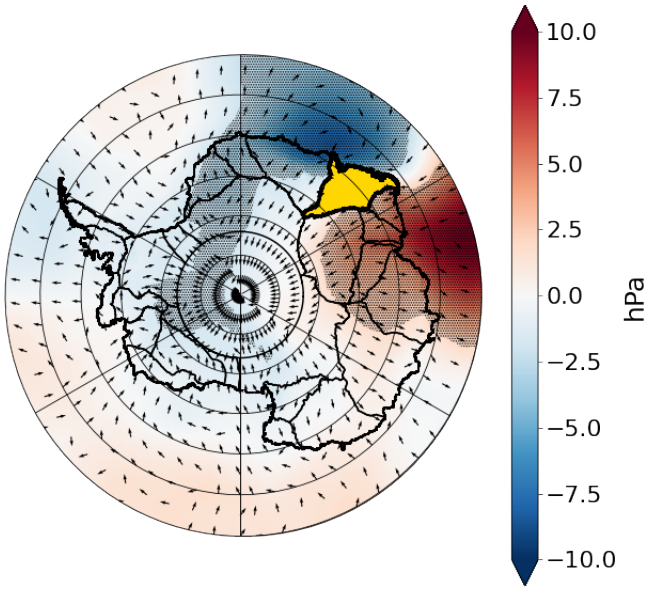

Figure 3.7: SLP anomalies for strong dipole regime example. Shaded areas represents statistically significant areas. Vectors represent surface wind anomalies. The yellow basin highlighted is the basin of interest.

highlighted as in the other regimes.

3.2.2 Water Vapor Analysis

Sea level pressure anomalies and wind anomaly patterns in the previous section alluded to moisture transport to the continent during extreme events. In order to further analyze moisture transport during extreme events, total precipitable water vapor anomalies were plotted for each basin, again during extreme cases.

Total precipitable water vapor anomalies are plotted for all twenty-five basins in Fig 3.10. Similar to Fig. 3.5, this figure shows positive anomalies in red and negative anomalies in blue with the basin of interest highlighted in yellow. Each subplot contains a colored border corresponding to the three sea level pressure regimes previ-

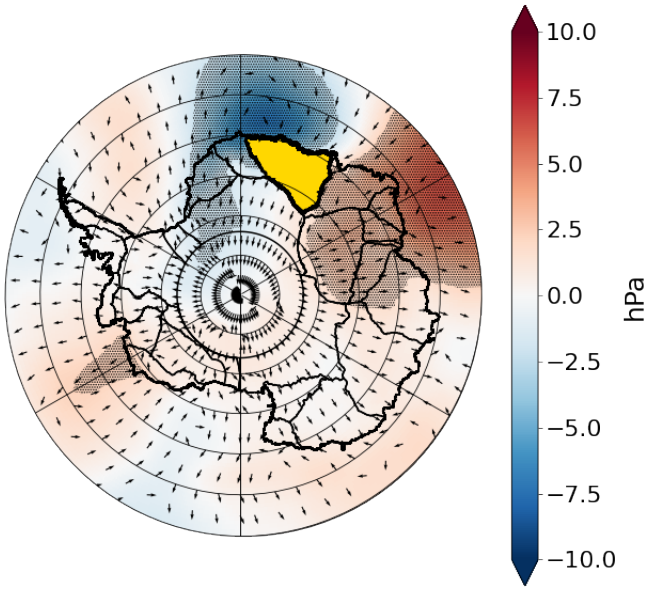

Figure 3.8: As in Fig. 3.7 but for weak regime

ously described. Nearly all basins experience positive total precipitable water vapor anomalies concentrated near the basin and surrounding ocean region. The magnitude and shape of the anomalies vary between basins. Some basins experience a concentrated narrow band of water vapor anomalies, while others have a more broad shape. These water vapor anomalies are found in between the high and low sea level pressure anomalies seen in Fig. 3.5. Paired with the surface wind anomalies, these vapor anomalies are transported towards the continent from the ocean. This enhanced water vapor transport found during extreme snowfall events is found across most basins on the AIS. This is consistent with the results found in limited basins in Rendfrey et al. (2024).

We would expect for a stronger sea level pressure dipole to bring more water vapor to the continent than a weaker dipole. To further explore this, we compared

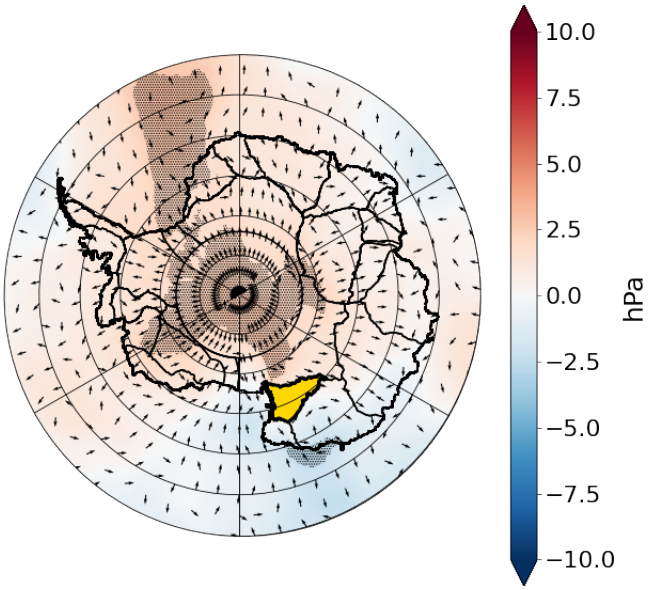

Figure 3.9: As in Fig. 3.7 but for no significant dipole

the maximum value of total precipitable water vapor anomalies for each basin and compared the basins in the three dipole regimes. The strong dipole basins had maximum TPWV anomalies of 2.25 kg/m2 or greater. Basins in the weak dipole regime had maximum TPWV anomalies between 1 and 2.25 kg/m2. Finally, basins with no significant dipole had maximum TPWV anomalies less than 1 kg/m2.

The difference in sea level pressure anomalies is plotted against the maximum total precipitable water vapor anomalies in Fig. 3.11. The linear regression line for the two variables is also plotted, the colors correspond to the sea level pressure regimes. The three regimes are apparent as clusters on the linear regression line. From the linear regression line, the relationship between the sea level dipole strength and the water vapor magnitude become clear. There is a positive correlation between sea level pressure difference and maximum TPWV. The R^2 value for this regression was

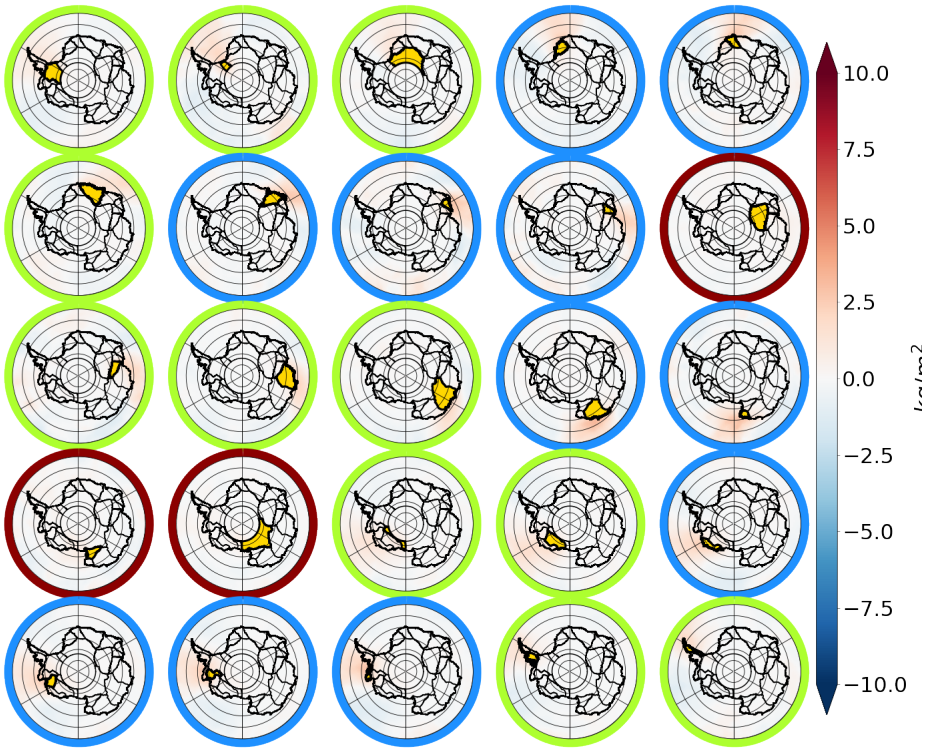

Figure 3.10: As in Fig. 3.5 but for TPWV

calculated to be 0.87, indicating a strong linear relationship between the two variables. This high R^2 value suggests that the variation in maximum total precipitable water vapor anomalies can be largely explained by the variation in sea level pressure anomalies, underscoring the significant role of sea level pressure dipoles in driving moisture transport to the continent during extreme snowfall events.

The relationship between maximum total precipitable water vapor (TPWV) anomalies and extreme snow rates is depicted in Fig. 3.12. In this plot, the maximum TPWV is on the x-axis and the extreme snow rates are on the y-axis. A positive correlation between these two variables is observed, indicating that higher

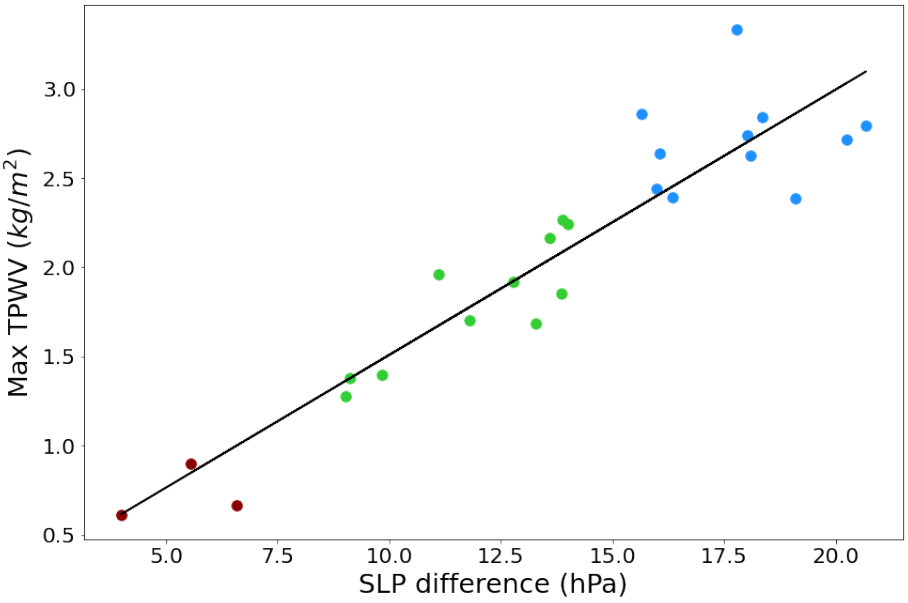

Figure 3.11: SLP difference vs Maximum TPWV. Basins with a strong dipole regime are colored in blue, the weak dipole regime green, and no dipole present red.

TPWV generally leads to higher extreme snow rates. However, the R^2 value for this regression is 0.46, suggesting that TPWV anomalies alone do not fully explain the variability in extreme snow rates. This lower R^2 value implies that other factors also significantly influence extreme snow rates. For instance, the presence of a dry layer in the atmosphere can inhibit the amount of snow that reaches the surface, despite high moisture availability aloft. Additionally, the efficiency of snow formation and precipitation processes, such as the availability of ice nuclei and the dynamics of cloud formation, can affect the conversion of water vapor to snowfall. These factors highlight the complexity of snowfall processes and indicate that while TPWV is an important driver, it is not the sole determinant of extreme snow rates.

3.2.3 Non-extreme Snow

To establish the extent to which these synoptic conditions are unique to extreme snow events, we calculated sea level pressure anomalies and total precipitable water

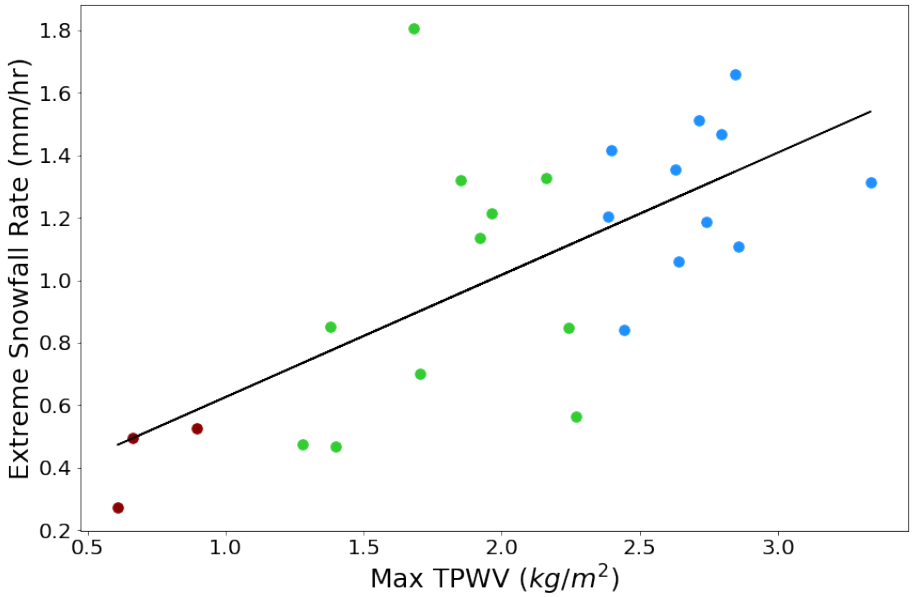

Figure 3.12: SLP difference vs Maximum TPWV. Basins with a strong dipole regime are colored in blue, the weak dipole regime green, and no dipole present red.

vapor anomalies for times experiencing median snow in each basin. Median snowfall is defined as snow rates between the 47.5th and 52.5th percentiles.

Although a sea level pressure dipole is still present in many basins during median snowfall events, it is significantly weaker than during extreme events. Using the same classification for dipole regimes as for extreme snow, only one basin (basin 23) barely qualifies for the weak SLP dipole regime, with an SLP difference of 8.51 hPa. This is demonstrated in 3.13, where all SLP differences are plotted for extreme and non-extreme snow. As seen from the figure, the SLP differences are significantly lower for non-extremes than extremes. Figure 3.14 displays SLP anomalies for median snowfall across all basins, showing that SLP dipoles are generally weak or absent in many basins.

Similarly, TPWV anomalies decrease substantially during median snowfall cases. On average, the maximum TPWV anomalies decrease by 3.5 kg/m2 for each basin. Figure 3.15 illustrates TPWV anomalies for median snowfall, indicating that while

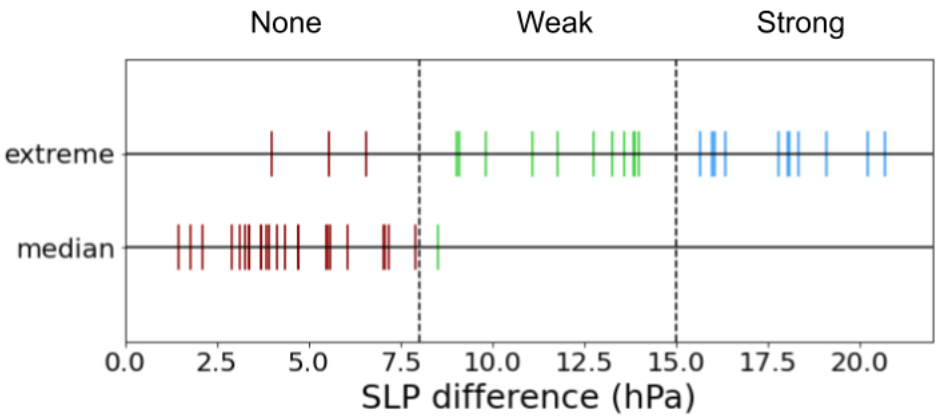

Figure 3.13: As in Fig. 3.6 but for non-extreme cases

positive TPWV anomalies are still present around the basins, their values are much lower compared to extreme snowfall cases.

Overall, the findings suggest that the synoptic patterns driving non-extreme snowfall events are similar to those causing extreme snowfall, but with significantly reduced intensity. Both sea level pressure dipoles and TPWV anomalies are much weaker during median snowfall events, indicating that while the same mechanisms are at play, their impact is less pronounced. This highlights the importance of understanding the intensity and magnitude of synoptic conditions in determining snowfall rates and accumulation in Antarctica.

3.2.4 AWS Analysis

To investigate extreme snow patterns at a local level and to provide independent confirmation of the satellite and reanalysis results, we performed AWS analysis using data from two AWS stations: Mizuho and Linda. Mizuho AWS is located in basin 7, while Linda AWS is situated in basin 17. Figure 3.16 shows the location of basin 7 and Mizuho AWS along with sea level pressure anomalies during extreme snowfall

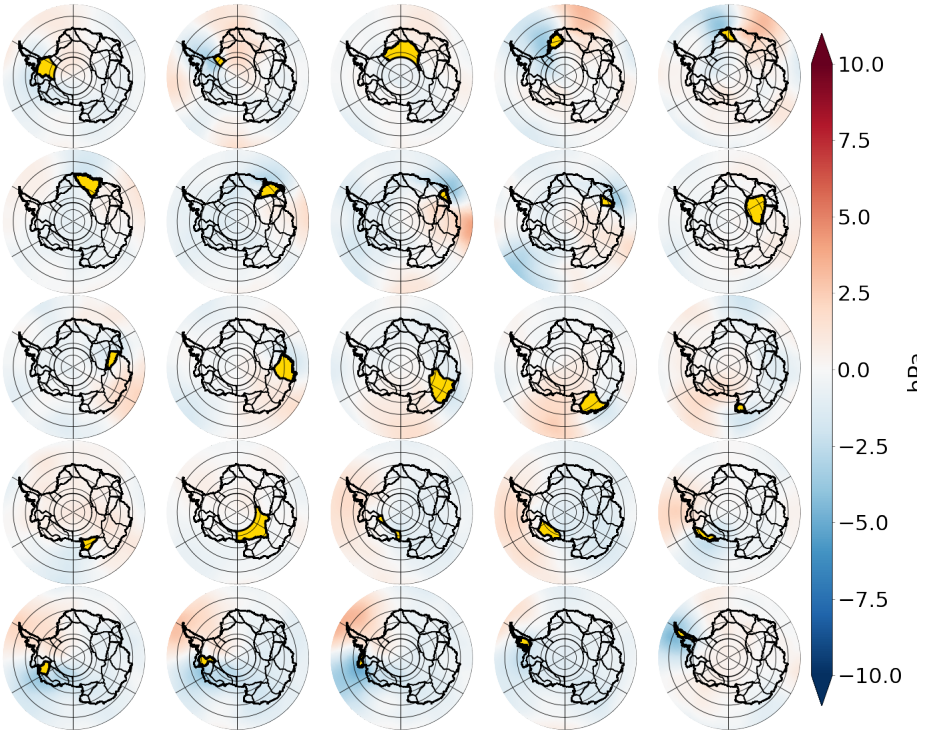

Figure 3.14: As in Fig. 3.5 but for non-extreme cases

events on the left. Similarly, the right panel illustrates the location of basin 17 and Linda AWS with corresponding sea level pressure anomalies.

These stations were chosen due to their contrasting conditions. Basin 7 exhibits a strong dipole regime during extreme events, while basin 17 shows no significant dipole. Unlike the strong dipole and weak dipole regimes explored in the previous section, basin 17 does not exhibit a low pressure system and a high pressure system near the basin. Instead, a low pressure system is seen near the basin, close to Linda AWS.

Additionally, Mizuho AWS is at an elevation of 2260 meters and further inland,

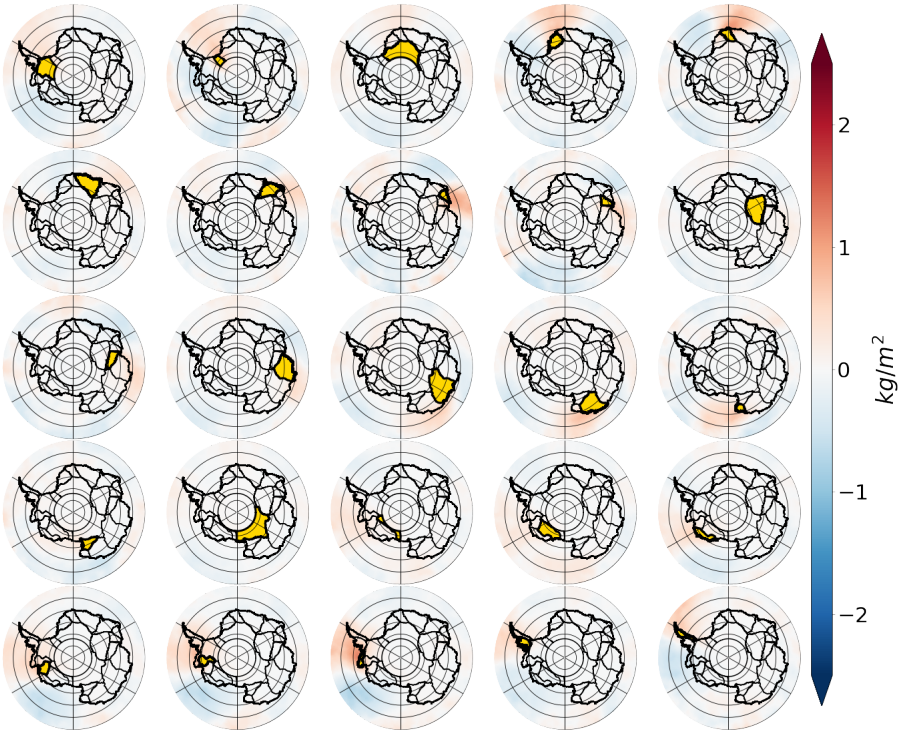

Figure 3.15: As in Fig. 3.10 but for non-extreme cases

whereas Linda AWS is only 46 meters above sea level and near the coast. By comparing these diverse conditions, we aim to understand how they influence extreme snowfall patterns in each region.

For Mizuho AWS, both extreme and non-extreme cases had a northerly component in the anomalous wind direction, which was consistent across nearly all cases analyzed. Temperature anomalies (top) and wind speed anomalies (bottom) for Mizuho AWS are shown in Figure 3.17. Histograms for extreme cases (pink) and non-extreme cases (green) demonstrate that temperatures during extreme snowfall events were significantly higher than those during non-extreme events at the 95%

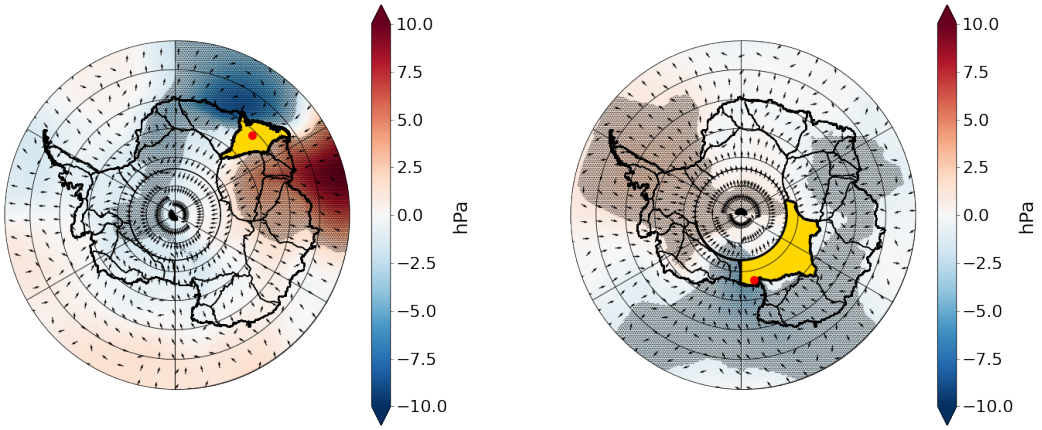

Figure 3.16: Locations of Mizuho AWS (left) and Linda AWS (right) shown in red with corresponding basins (yellow) and SLP anomalies as in Fig. 3.7.

confidence level. Similarly, wind speed anomalies were greater during extreme cases, also significant at the 95% confidence level.

At Linda AWS, a similar pattern emerged with both extreme and non-extreme cases exhibiting a northerly wind anomaly. Figure 3.18 presents temperature anomalies (top) and wind speed anomalies (bottom) for Linda AWS. Again, histograms for extreme cases (pink) and non-extreme cases (green) indicate that temperatures and wind speeds during extreme snowfall events were significantly higher than during non-extreme events, both statistically significant at the 95% confidence level.

Despite the differences in regimes driving extreme events at Mizuho and Linda AWS, both stations show evidence of warm, moist air being transported to the station during extreme events. This transport of warm, moist air is a key driver of extreme snowfall in both regions, highlighting the significance of atmospheric moisture and wind patterns in influencing snowfall rates across diverse climatological conditions.

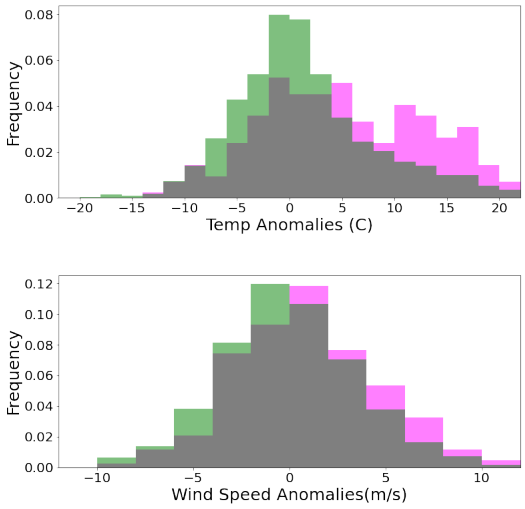

Figure 3.17: Histogram of temperature (Top) and wind speed (bottom) at Mizuho AWS. Extreme snow is shown in pink and non-extreme snow is shown in green.

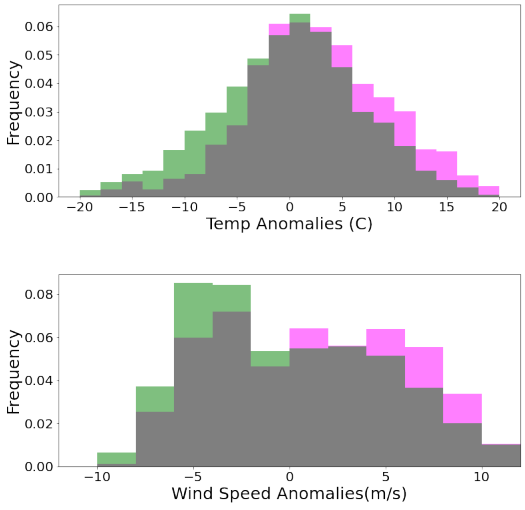

Figure 3.18: As in Fig. 3.17 but for Linda AWS.

Chapter 4

Summary

4.1 Conclusion

The new Combined CloudSat CALIPSO Snow (C3S) product was used to identify extreme snowfall and evaluate their contributions to the ice mass of the Antarctic ice sheet (AIS). Additionally, MERRA-2 reanalysis and AWS observations were used to examine the atmospheric conditions cause extreme snow and how this differs across the continent.

Extreme snowfall is found to exert a significant contribution to the AIS ice mass. The 95th percentile snow rate for the entire continent is 0.57 mm/hr, with lower rates in interior basins and higher rates in coastal regions. Extreme snowfall accounts for approximately 40% of the total accumulation across Antarctica. When examined by basin, extreme snowfall predominantly occurs near the coasts in the East Antarctic Ice Sheet (EAIS), while in the West Antarctic Ice Sheet (WAIS), extreme events are more dispersed. The fraction of accumulation from extreme snowfall is higher in the EAIS than in the WAIS, reflecting the differing distributions of snowfall events. However, the snow rate threshold for extreme snowfall does not exhibit the same

spatial pattern, with basins at lower elevations and closer to the coast experiencing higher snow rates, as depicted in Fig. 3.1. This indicates that extreme events are more frequent in lower elevation regions.

Similar to the findings for the 95th percentile snow rates, the snow rates that account for half of the accumulation are also higher in basins located in coastal regions with lower average elevations. However, the specific percentiles that contribute to half of the total accumulation do not follow the same consistent spatial pattern as the 95th percentile snow rates. This discrepancy indicates that the behavior of snowfall accumulation varies significantly between different percentiles across the basins, highlighting distinct accumulation dynamics between the 95th percentile and lower percentiles.

Previous studies, such as Wang et al. (2023), have shown that extreme events are crucial to surface mass balance, this analysis further highlights the significance of extreme snowfall in contributing to snowfall accumulation in each basin. Extreme snowfall from all basins collectively contributes 476 gigatons per year to the AIS, representing about 36% of the total ice mass contributions from snow, which is nearly four times higher than the estimated annual ice loss of 120 gigatons. These findings underscore the importance of studying extreme snowfall and its variability, given the substantial impact on the ice sheet's mass balance.

We found that for extreme events, most basins exhibit a sea level pressure (SLP) dipole pattern, characterized by a low-pressure anomaly to the west and a high-pressure anomaly to the east of the basin. This dipole pattern can be classified into three regimes: strong dipole (11 basins), weak dipole (11 basins), and no significant dipole (3 basins). The SLP dipole, combined with wind speed and direction data, indicates enhanced water vapor transport towards the continent, facilitating extreme precipitation events.

Furthermore, nearly all basins experience positive total precipitable water vapor (TPWV) anomalies during extreme snowfall events, concentrated near the respective basins. A positive correlation between maximum TPWV anomalies and the SLP dipole index was observed, suggesting that as the difference between SLP extremes increases, TPWV anomalies also increase. Additionally, a positive correlation was found between TPWV anomalies and the extreme snow rates. This correlation supports the notion that the SLP dipole effectively channels moisture towards the continent, enhancing precipitation.

AWS data further confirms that at a local level, moisture is transported to the continent which is reflected in temperature, wind speed, and wind direction.

Extreme snowfall can mitigate the effects of melting ice sheets on sea level rise, contributing about 40% of the accumulation on the Antarctic ice sheet. In agreement with previous studies, extreme snow is caused by a sea level pressure dipole which funnels moisture towards the continent. Unlike other studies, this analysis shows that this pattern is found across most basins in Antarctica as opposed to a few select regions that focus on water vapor transport.

4.2 Future Work

The C3S product, like other satellite products, only gives us a snapshot of the precipitation on the continent. This analysis focused on the atmospheric features during corresponding snapshots from the C3S product. However, atmospheric processes are dynamic and studying the temporal evolution of these features is imperative for truly understanding them.

Additionally, this work is limited in the synoptic analysis done for extreme snowfall cases. In order to further diagnose these events, further analysis should be per-

formed to look at varying levels of the atmosphere, not just the surface. This will give us further insight into how moisture is transported to the Antarctic Ice Sheet (AIS). Analyzing moisture levels at different atmospheric layers is crucial from a cloud physics perspective, as it helps determine where clouds and precipitation may form, how they will develop, and how they will precipitate. Understanding these dynamics is essential for predicting weather patterns and assessing the impact of atmospheric moisture on precipitation processes in Antarctica. Furthermore, studying the levels of moisture in the atmosphere is important for understanding ice crystal formation and growth. These growth processes are highly dependent on the available moisture and temperature conditions. This knowledge can enhance our predictions of snowfall rates and patterns, which are critical for understanding and modeling the Antarctic climate system.

While the C3S product has shown to be a useful tool in measuring snowfall across the AIS, where in situ measurements are difficult and rare, the time constraint of just four years is limiting. Additionally, while it is important to study past observations in order to study change in the future, these A-train measurements are 15 years old. However with the launch of the European Space Agency's EarthCare Satellite in May 2024, a new opportunity arises. Similar to CloudSat and CALIPSO, EarthCare is equipped with a Cloud Profiling Radar and Lidar with the potential to measure precipitation over the poles. This provides the opportunity to compare C3S observations with measurements from the new instrument. This comparison of a 15 year difference, may give us insight into how snowfall has changed over the AIS over the past 15 years and how it may evolve in the near future.

Lastly, it may be of interest to evaluate our results in climate models. This work would compliment the work of Palerme et al. (2017), which evaluated current and projected snow on the AIS and Pendergrass and Knutti (2018), which evaluated the

results of extreme rainfall in model projections. It would first be important to compare if models capture the same 95th percentile snowfall intensities and contributions to total accumulation during the same time period as this study. Furthermore, we could then look into how the SLP and TPWV results differ from this study. Finally, we could look at future projections to evaluate how much the 95th percentile snow is changing.

Bibliography

AMRDC, A. M. R. a. D. C., 2022: Automatic Weather Station project data, 1980 - present (ongoing). AMRDC Data Repository, URL https://amrdcdata.ssec.wisc.edu/group/about/automatic-weather-station-project, doi:10.48567/1HN2-NW60.

Cao, Q., Y. Hong, S. Chen, J. J. Gourley, J. Zhang, and P. E. Kirstetter, 2014: Snowfall Detectability of NASA'S CloudSat: The firt cross-investigation of its 2C-SNOW-PROFILE product and national multi-sensor MOSAIC QPE (NMQ) snowfall data. *Progress In Electromagnetics Research*, **148**, 55–61, doi:10.2528/PIER14030405.

Chen, S., and Coauthors, 2016: Comparison of snowfall estimates from the NASA CloudSat Cloud Profiling Radar and NOAA/NSSL Multi-Radar Multi-Sensor System. *Journal of Hydrology*, **541**, 862–872, doi:10.1016/j.jhydrol.2016.07.047.

Church, J., and Coauthors, 2013: "Chapter 13: Sea Level Change" in Climate Change 2013: The Physical Science Basis: Contribution of Working Group I to the Fifth Assessment Report of the Intergovernmental Panel on Climate Change. *State & Federal Reports and Publications*.

Clem, K. R., and Coauthors, 2023: Antarctica and the Southern Ocean. doi:10.1175/BAMS-D-23-0077.1.

Dangendorf, S., C. Hay, F. M. Calafat, M. Marcos, C. G. Piecuch, K. Berk, and J. Jensen, 2019: Persistent acceleration in global sea-level rise since the 1960s. *Nature Climate Change*, **9 (9)**, 705–710, doi:10.1038/s41558-019-0531-8.

De Leo, F., S. A. Talke, P. M. Orton, and T. Wahl, 2022: The Effect of Harbor Developments on Future High-Tide Flooding in Miami, Florida. *Journal of Geophysical Research: Oceans*, **127 (7)**, e2022JC018 496, doi:10.1029/2022JC018496.

Frederikse, T., and Coauthors, 2020: The causes of sea-level rise since 1900. *Nature*, **584 (7821)**, 393–397, doi:10.1038/s41586-020-2591-3.

Frieler, K., and Coauthors, 2015: Consistent evidence of increasing Antarctic accumulation with warming. *Nature Climate Change*, **5 (4)**, 348–352, doi:10.1038/nclimate2574.

Gardner, A. S., G. Moholdt, T. Scambos, M. Fahnstock, S. Ligtenberg, M. van den Broeke, and J. Nilsson, 2018: Increased West Antarctic and unchanged East Antarctic ice discharge over the last 7 years. *The Cryosphere*, **12 (2)**, 521–547, doi:10.5194/tc-12-521-2018.

Gelaro, R., and Coauthors, 2017: The Modern-Era Retrospective Analysis for Research and Applications, Version 2 (MERRA-2). *Journal of climate*, **Volume 30 (Iss 13)**, 5419–5454, doi:10.1175/JCLI-D-16-0758.1.

Gimeno, L., R. Nieto, M. Vázquez, and D. A. Lavers, 2014: Atmospheric rivers: a mini-review. *Frontiers in Earth Science*, **2**, doi:10.3389/feart.2014.00002.

González Herrero, S., F. Vasallo, J. Bech, I. Gorodetskaya, B. Elvira Montejo, and A. Justel, 2023: Extreme precipitation records in Antarctica.

Gorodetskaya, I. V., M. Tsukernik, K. Claes, M. F. Ralph, W. D. Neff, and N. P. M. Van Lipzig, 2014: The role of atmospheric rivers in anomalous snow accumulation in East Antarctica. *Geophysical Research Letters*, **41 (17)**, 6199–6206, doi:10.1002/2014GL060881.

Grazioli, J., J.-B. Madeleine, H. Gallée, R. M. Forbes, C. Genthon, G. Krinner, and A. Berne, 2017: Katabatic winds diminish precipitation contribution to the Antarctic ice mass balance. *Proceedings of the National Academy of Sciences*, **114 (41)**, 10 858–10 863, doi:10.1073/pnas.1707633114.

Hay, C. C., E. Morrow, R. E. Kopp, and J. X. Mitrovica, 2015: Probabilistic reanalysis of twentieth-century sea-level rise. *Nature*, **517 (7535)**, 481–484, doi:10.1038/nature14093.

Helm, V., A. Humbert, and H. Miller, 2014: Elevation and elevation change of Greenland and Antarctica derived from CryoSat-2. *The Cryosphere*, **8 (4)**, 1539–1559, doi:10.5194/tc-8-1539-2014.

Henderson, D. S., T. L'Ecuyer, G. Stephens, P. Partain, and M. Sekiguchi, 2013: A Multisensor Perspective on the Radiative Impacts of Clouds and Aerosols. doi:10.1175/JAMC-D-12-025.1.

Joughin, I., B. E. Smith, and B. Medley, 2014: Marine Ice Sheet Collapse Potentially Under Way for the Thwaites Glacier Basin, West Antarctica. *Science*, **344 (6185)**, 735–738, doi:10.1126/science.1249055.

Lazzara, M. A., G. A. Weidner, L. M. Keller, J. E. Thom, and J. J. Cassano, 2012: Antarctic Automatic Weather Station Program: 30 Years of Polar Observation. doi:10.1175/BAMS-D-11-00015.1.

L'Ecuyer, T. S., N. B. Wood, T. Haladay, G. L. Stephens, and P. W. Stackhouse Jr., 2008: Impact of clouds on atmospheric heating based on the R04 CloudSat fluxes and heating rates data set. *Journal of Geophysical Research: Atmospheres*, **113 (D8)**, doi:10.1029/2008JD009951.

Lemonnier, F., and Coauthors, 2019: Evaluation of CloudSat snowfall rate profiles by a comparison with in situ micro-rain radar observations in East Antarctica. *The Cryosphere*, **13 (3)**, 943–954, doi:10.5194/tc-13-943-2019.

Liu, G., 2008: Deriving snow cloud characteristics from CloudSat observations. *Journal of Geophysical Research: Atmospheres*, **113 (D8)**, doi:10.1029/2007JD009766.

L'Ecuyer, T. S., and J. H. Jiang, 2010: Touring the atmosphere aboard the A-Train. *Physics Today*, **63 (7)**, 36–41, doi:10.1063/1.3463626.

Mace, G. G., and Q. Zhang, 2014: The CloudSat radar-lidar geometrical profile product (RL-GeoProf): Updates, improvements, and selected results. *Journal of Geophysical Research: Atmospheres*, **119 (15)**, 9441–9462, doi:10.1002/2013JD021374.

Maclennan, M. L., J. T. M. Lenaerts, C. Shields, and J. D. Wille, 2022: Contribution of Atmospheric Rivers to Antarctic Precipitation. *Geophysical Research Letters*, **49 (18)**, e2022GL100 585, doi:10.1029/2022GL100585.

Medley, B., and E. R. Thomas, 2019: Increased snowfall over the Antarctic Ice Sheet mitigated twentieth-century sea-level rise. *Nature Climate Change*, **9 (1)**, 34–39, doi:10.1038/s41558-018-0356-x.

Milani, L., and N. B. Wood, 2021: Biases in CloudSat Falling Snow Estimates Resulting from Daylight-Only Operations. *Remote Sensing*, **13 (11)**, 2041, doi:10.3390/rs13112041.

Mroz, K., M. Montopoli, A. Battaglia, G. Panegrossi, P. Kirstetter, and L. Baldini, 2021: Cross Validation of Active and Passive Microwave Snowfall Products over the Continental United States. doi:10.1175/JHM-D-20-0222.1.

Norin, L., A. Devasthale, T. S. L'Ecuyer, N. B. Wood, and M. Smalley, 2015: Intercomparison of snowfall estimates derived from the CloudSat Cloud Profiling Radar and the ground-based weather radar network over Sweden. *Atmospheric Measurement Techniques*, **8 (12)**, 5009–5021, doi:10.5194/amt-8-5009-2015.

Oppenheimer, M., and Coauthors, 2019: Sea level rise and implications for low lying islands, coasts and communities.

Palerme, C., C. Claud, N. B. Wood, T. L'Ecuyer, and C. Genthon, 2019: How Does Ground Clutter Affect CloudSat Snowfall Retrievals Over Ice Sheets? *IEEE Geoscience and Remote Sensing Letters*, **16 (3)**, 342–346, doi:10.1109/LGRS.2018.2875007.

Palerme, C., C. Genthon, C. Claud, J. E. Kay, N. B. Wood, and T. L'Ecuyer, 2017: Evaluation of current and projected Antarctic precipitation in CMIP5 models. *Climate Dynamics*, **48 (1)**, 225–239, doi:10.1007/s00382-016-3071-1.

Palerme, C., J. E. Kay, C. Genthon, T. L'Ecuyer, N. B. Wood, and C. Claud, 2014: How much snow falls on the Antarctic ice sheet? *The Cryosphere*, **8 (4)**, 1577–1587, doi:10.5194/tc-8-1577-2014.

Palm, S. P., V. Kayetha, Y. Yang, and R. Pauly, 2017: Blowing snow sublimation and transport over Antarctica from 11 years of CALIPSO observations. *The Cryosphere*, **11 (6)**, 2555–2569, doi:10.5194/tc-11-2555-2017.

Palm, S. P., Y. Yang, J. D. Spinhirne, and A. Marshak, 2011: Satellite remote sensing of blowing snow properties over Antarctica. *Journal of Geophysical Research: Atmospheres*, **116 (D16)**, doi:10.1029/2011JD015828.

Parish, T. R., and J. J. Cassano, 2003: The Role of Katabatic Winds on the Antarctic Surface Wind Regime.

Pendergrass, A. G., and R. Knutti, 2018: The Uneven Nature of Daily Precipitation and Its Change. *Geophysical Research Letters*, **45 (21)**, 11,980–11,988, doi:10.1029/2018GL080298.

Rendfrey, T. S., C. Pettersen, J. N. Bassis, and M. E. Mateling, 2024: CloudSat Observations Show Enhanced Moisture Transport Events Increase Snowfall Rate and Frequency Over Antarctic Ice Sheet Basins. *Journal of Geophysical Research: Atmospheres*, **129 (6)**, e2023JD040 556, doi:10.1029/2023JD040556.

Rignot, E., J. Mouginot, M. Morlighem, H. Seroussi, and B. Scheuchl, 2014: Widespread, rapid grounding line retreat of Pine Island, Thwaites, Smith, and Kohler glaciers, West Antarctica, from 1992 to 2011. *Geophysical Research Letters*, **41 (10)**, 3502–3509, doi:10.1002/2014GL060140.

Rignot, E., I. Velicogna, M. R. van den Broeke, A. Monaghan, and J. T. M. Lenaerts, 2011: Acceleration of the contribution of the Greenland and Antarctic ice sheets to sea level rise. *Geophysical Research Letters*, **38 (5)**, doi:10.1029/2011GL046583.

Sassen, K., Z. Wang, and D. Liu, 2008: Global distribution of cirrus clouds from CloudSat/Cloud-Aerosol Lidar and Infrared Pathfinder Satellite Observations (CALIPSO) measurements. *Journal of Geophysical Research: Atmospheres*, **113 (D8)**, doi:10.1029/2008JD009972.

Shepherd, A., and Coauthors, 2012: A Reconciled Estimate of Ice-Sheet Mass Balance. *Science*, **338 (6111)**, 1183–1189, doi:10.1126/science.1228102.

Shepherd, A., and Coauthors, 2019: Trends in Antarctic Ice Sheet Elevation and Mass. *Geophysical Research Letters*, **46 (14)**, 8174–8183, doi:10.1029/2019GL082182.

Smith, B., and Coauthors, 2020: Pervasive ice sheet mass loss reflects competing ocean and atmosphere processes. *Science*, **368 (6496)**, 1239–1242, doi:10.1126/science.aaz5845.

Souverijns, N., and Coauthors, 2018: Evaluation of the CloudSat surface snowfall product over Antarctica using ground-based precipitation radars. *The Cryosphere*, **12 (12)**, 3775–3789, doi:10.5194/tc-12-3775-2018.

Stephens, G. L., and T. D. Ellis, 2008: Controls of Global-Mean Precipitation Increases in Global Warming GCM Experiments. doi:10.1175/2008JCLI2144.1.

Tanelli, S., S. L. Durden, E. Im, K. S. Pak, D. G. Reinke, P. Partain, J. M. Haynes, and R. T. Marchand, 2008: CloudSat's Cloud Profiling Radar After Two Years in Orbit: Performance, Calibration, and Processing. *IEEE Transactions on Geoscience and Remote Sensing*, **46 (11)**, 3560–3573, doi:10.1109/TGRS.2008.2002030.

Turner, J., and Coauthors, 2019: The Dominant Role of Extreme Precipitation Events in Antarctic Snowfall Variability. *Geophysical Research Letters*, **46 (6)**, 3502–3511, doi:10.1029/2018GL081517.

Wang, W., Y. Shen, Q. Chen, and F. Wang, 2023: Unprecedented mass gain over the Antarctic ice sheet between 2021 and 2022 caused by large precipitation anomalies. *Environmental Research Letters*, **18 (12)**, 124 012, doi:10.1088/1748-9326/ad0863.

Wendler, G., C. Stearns, G. Weidner, G. Dargaud, and T. Parish, 1997: On the extraordinary katabatic winds of Adélie Land. *Journal of Geophysical Research: Atmospheres*, **102 (D4)**, 4463–4474, doi:10.1029/96JD03438.

Wille, J. D., and Coauthors, 2024: The Extraordinary March 2022 East Antarctica "Heat" Wave. Part II: Impacts on the Antarctic Ice Sheet. doi:10.1175/JCLI-D-23-0176.1.

Winker, D. M., M. A. Vaughan, A. Omar, Y. Hu, K. A. Powell, Z. Liu, W. H. Hunt, and S. A. Young, 2009: Overview of the CALIPSO Mission and CALIOP Data Processing Algorithms. doi:10.1175/2009JTECHA1281.1.

Wood, N., and T. L'Ecuyer, 2018: Level 2C Snow Profile Process Description and Interface Control Document. URL https://www.cloudsat.cira.colostate.edu/data-products/2c-snow-profile.

Wood, N. B., and T. S. L'Ecuyer, 2021: What millimeter-wavelength radar reflectivity reveals about snowfall: an information-centric analysis. *Atmospheric Measurement Techniques*, **14 (2)**, 869–888, doi:10.5194/amt-14-869-2021.

Zwally, H. J., M. B. Giovinetto, M. A. Beckley, and J. L. Saba, 2012: Antarctic and Greenland Drainage Systems. GSFC Cryospheric Sciences Laboratory, URL https://earth.gsfc.nasa.gov/cryo/data/polar-altimetry/antarctic-and-greenland-drainage-systems.